the 10 subjects acquired simultaneously with a gap of 0.1 second starting from time t= 0 to 0.6 seconds. All images were identified as $I_N^{AP}(x, y, t)$ where $\{N, t \in \mathbb{R}^+ | 1 \leq N \leq 10, 0.1 \leq t \leq 1\}$ and (x, y) are the coordinates in the Cartesian plane, t being the timestamp at which the particular frame/image was recorded, N would be the number assigned to the test subject and AP signifies the three anatomical planes of view i.e. Axial (a), Coronal (c) and Sagittal (s). So, the sixth subject's Coronal CT image acquired at t=0.3 sec would be identified as $I_6^c(x, y, 0.3)$. Samples of images used from all viewpoints and all subjects from timestamps 0.1 to 0.6 seconds are summarized in Table 4.1.

Table 4.1: Working database through all anatomical planes from t=0.1 to 0.6 sec

	Axial	Coronal	Sagittal
1	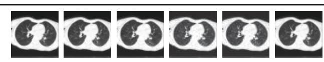	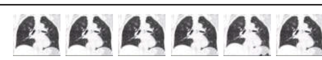	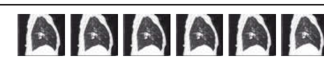
2	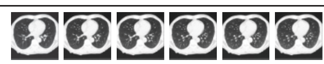	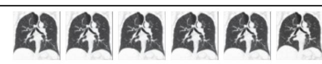	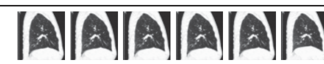
3	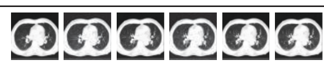		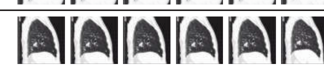
4	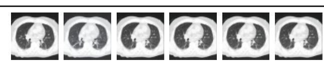	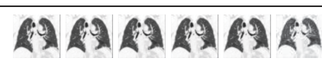	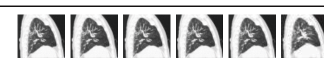
5	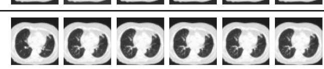	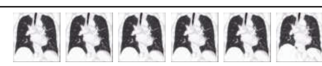	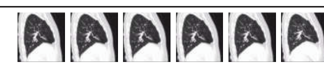
6	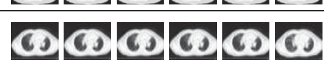		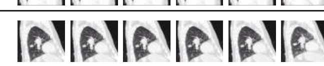
7	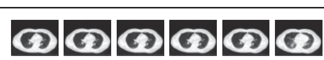		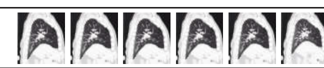
8	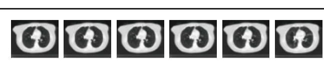	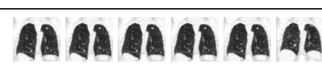	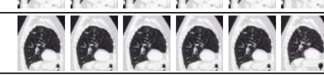
9	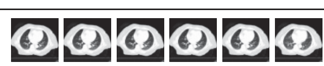	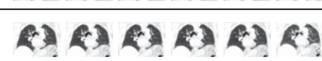	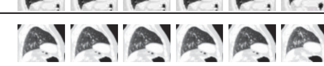
10	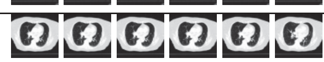	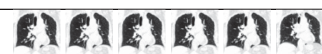	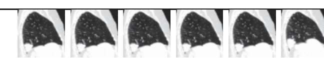

4.3.2 Proposed Methodology

The procedure acquired is as such that a temporal thoracic image sequence from time t=0.1 to 0.6 sec is taken such that first frame of the sequence is the full inhale frame and the last frame is full exhale frame. This paper uses the Speeded up

Robust Feature detector (SURF) [Bay, H. *et al.*, 2006, 2008] to obtain a feature set comprising of common feature points throughout the image sequence. It detects and describes the feature set irrespective of any scaling and /or rotation in the corresponding images. SURF provides better approximations in comparison to previously proposed schemes with respect to repeatability, distinctiveness, and robustness, yet can be computed and compared much faster than any other state of the art feature detector. These feature sets are then fed into the OFM estimation algorithm to identify the deformation path throughout the temporal sequence, be it peripheral or local.

Optical flow has been successfully applied to motion estimation of points/point clouds and other point set surface definitions over a temporal sequence [Sun, D. *et al.*, 2014]. It performs better than its contemporaries while tracing deformations that are realistic and guides the user in manipulation of real-world objects. It also allows the user to specify the deformations using either sets of points or line segments, the later useful for controlling curves and profiles present in the image. For each of these techniques, it provides simple closed-form solutions that yield fast deformations, which can be performed in real-time. The proposed methodology aims to track and estimate the deformations by tracking the transition of the interest points through the sequence from full inhale to full exhale frame. The overall process can be referred to in Figure 4.1.

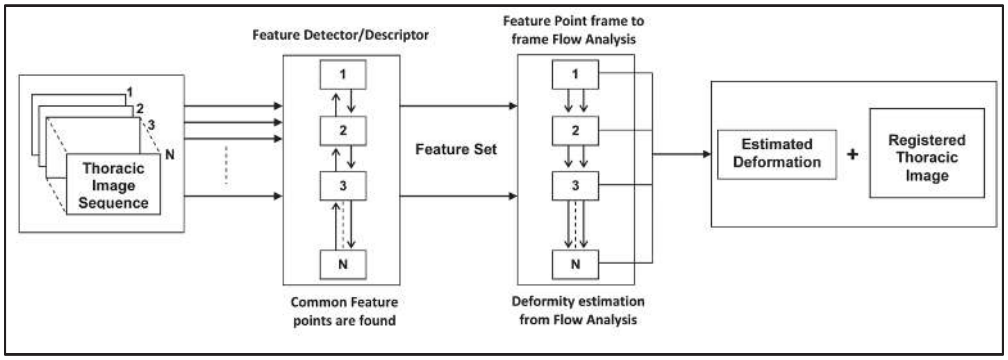

Figure 4.1: The proposed framework structure

A novel scale- and rotation-invariant detector and descriptor, has been coined as Speeded-Up Robust Features (SURF) by Herbert Bay et.al in 2006 [Bay, H. *et al.*, 2006] and 2008 [Bay, H. *et al.*, 2008]. It provides better approximations in comparison to previously proposed schemes with respect to repeatability, distinctiveness, and robustness, yet can be computed and compared much faster. Focus is on scale and in-plane rotation-invariant detection and descriptions. These seem to offer a good compromise between feature complexity and robustness to commonly occurring photometric deformations in thoracic images. Skewing, anisotropic scaling, and perspective effects are assumed to be second order effects, that are covered to some degree by the overall robustness of the descriptor. For guaranteed invariance to any scale changes the input thoracic images are analyzed at different scales. The detected interest points are provided with a rotation and scale-invariant descriptor. The detector is based on Hessian matrix based on its good performance in accuracy [Bay, H. *et al.*, 2008]. Blob-like structures are detected at locations with maximum determinant. In comparison to the Hessian-Laplace detector [Mikolajczyk, K. & Schmid, C., 2001] Hessian determinant is used for scale selection [Lindeberg, T., 1998].

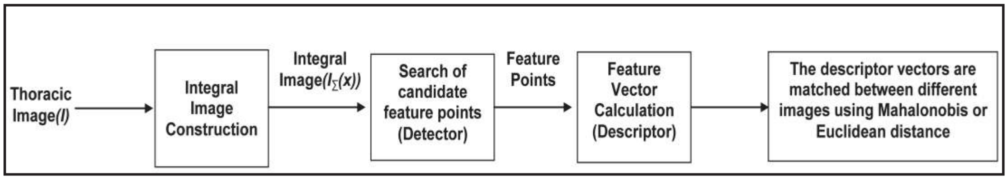

Figure 4.2: The working model of SURF

Given a point ***a*** = *(x, y)* in an image I_N^{AP}, the Hessian matrix $\hat{H}(\boldsymbol{a}, \sigma)$ at scale σ is defined as follows

$$\hat{H}(a,\sigma) = \begin{bmatrix} L_{xx}(a,\sigma) & L_{xy}(a,\sigma) \\ L_{xy}(a,\sigma) & L_{yy}(a,\sigma) \end{bmatrix} \tag{4.1}$$

where $L_{xx}(a,\sigma)$ is the convolution of the Gaussian second derivative $\partial g(\sigma) / \partial a^2$ with the image I_N^{AP} at point ***a***, similarly for $L_{xy}(a,\sigma)$ and $L_{yy}(a,\sigma)$.

Though, Gaussians are optimal for scale-space analysis [Koenderink, J. J., 1984], they have to be made discrete and cropped in practice. This results in loss in repeatability of the detector for thoracic CT image rotations around odd multiples of π/4.

The SURF method consists of multiple stages to obtain relevant feature points from a sequence of thoracic images. The single SURF stages are (as shown in fig 4.2):

1. An integral image is constructed for each frame of the input thoracic image sequence, it allows for fast computation of box type convolution filters [Viola, P. & Jones, M., 2001]. This enables very few memory

accesses and hence results in drastic improvement in computational time [Cornelis, N. & Gool, L. V., 2008], which is especially crucial when we are dealing with a sequence of images. An integral image $I_{N\ \Sigma}^{AP}(a)$ at a location ***a***= (x, y)^T represents the sum of all pixels in the input image I_N^{AP} within a rectangular region formed by the origin and ***a***

$$I_{N\ \Sigma}^{AP}(a) = \sum_{i=0}^{i \le x} \sum_{j=0}^{j \le y} I_N^{AP}(i, j) \tag{4.2}$$

2. Candidate feature points are searched by the creation of a Hessian scale-space pyramid (SURF detector). Approximation of the Hessian as a combination of box filters allows fast filtering. High contrast feature points are selected.
3. Feature vector is calculated (SURF descriptor) based on its characteristic direction to provide rotation invariance. Feature vector is normalized for immunity to changes in lighting conditions.
4. Matching of descriptor vectors between the thoracic image sequence frames using distance measures such as Mahalonobis distance and Euclidean distances etc.

Optical flow is the pattern of apparent motion of objects, surfaces, and edges in a visual scene caused by the relative motion between an observer (an eye or a camera) and the scene [Warren, D. H. & Strelow, E. R., 1985]. In recent times, the term optical flow has been co-opted by computer vision experts to incorporate related techniques from image processing and control of navigation, such as motion detection, object segmentation, time-to-contact information, focus of expansion calculations, luminance and motion compensated encoding and stereo disparity measurement [Beauchemin, S. S. & Barron, J. L., 1995]. Sequences of ordered thoracic images allow the estimation of motion as either instantaneous image velocities or discrete image displacements [Aires, K. R. *et al.*, 2008]. Barron et.al provided a performance analysis of a number of optical flow techniques. It emphasizes the accuracy and density of measurements [Barron, J. L. et al., 1994].

Suppose we have a continuous thoracic image frame $I_N^{AP}(x, y, t)$; $f(x, y, t)$ refers to the gray-level of (x, y) at time t. It represents a dynamic thoracic image as a function of position and time. Few assumptions also work in hindsight:

- The detected feature point moves but does not actually change intensity.
- Feature point at location (x, y) in frame i is the feature point at (x+Δx, y+Δy) in frame *i+1* (detailed in figure 4.3).

For making computation simpler and quicker the real world three dimensional (3-D+time) objects are transferred to a (2-D+time) case. Then the thoracic image can be described by the 2-D dynamic brightness function of $I(x, y, t)$. Provided that in the neighbourhood of the feature point, change of brightness intensity does not happen in the motion field, following expression can be used:

$$I(x, y, t) = I(x + \delta x, y + \delta y, t + \delta t) \tag{4.3}$$

Taylor series is used for the right-hand side of the above equation, to obtain

$$I(x + \delta x, y + \delta y, t + \delta t) = I(x, y, t) + \frac{\partial I}{\partial x}\Delta x + \frac{\partial I}{\partial y}\Delta y + \frac{\partial I}{\partial t}\Delta t + \text{Higher order terms} \tag{4.4}$$

From equations 4.3 and 4.4; neglecting the higher order terms,

$$\frac{\partial I}{\partial x}\Delta x + \frac{\partial I}{\partial y}\Delta y + \frac{\partial I}{\partial t}\Delta t = 0 \qquad (4.5)$$

Dividing the terms in equation 4.5 by Δt on both sides (to get the equation in terms of x, y component velocity)

$$\frac{\partial I}{\partial x}{}^{\Delta x}\!\!/_{\Delta t} + \frac{\partial I}{\partial y}{}^{\Delta y}\!\!/_{\Delta t} + \frac{\partial I}{\partial t} = 0 \qquad (4.6)$$

where ${}^{\Delta x}\!/_{\Delta t} = V_x, {}^{\Delta y}\!/_{\Delta t} = V_y$; thus,

$$\frac{\partial I}{\partial x}V_x + \frac{\partial I}{\partial y}V_y + \frac{\partial I}{\partial t} = 0 \qquad (4.7)$$

Where V_x and V_y are the x and y components of velocity or optical flow of $I(x, y, t)$; $\frac{\partial I}{\partial x}$, $\frac{\partial I}{\partial y}$ and $\frac{\partial I}{\partial t}$ being the spatio-temporal derivatives of $I(x, y, t)$

$$I_x.v_x + I_y.v_y = -I_t \qquad (4.8)$$

Vector representation being

$$\nabla I.\vec{v} == -I_t \qquad (4.9)$$

Where ∇I is the spatial gradient of brightness intensity and $\vec{v}$ is the optical flow (velocity vector) of the previously detected feature points, I_t being the time derivative of the brightness intensity.

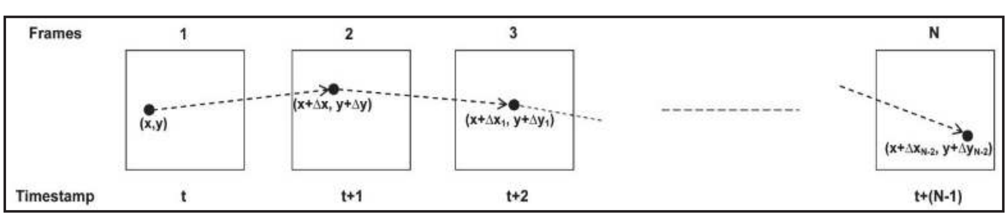

Figure 4.3: Flow of a common feature point (x, y) through a sequentially temporal thoracic image sequence with N frames, arrows indicate the changing velocity vector $\vec{v}$

4.4 Results and Discussion

The feature detector/descriptor implemented on the temporal image sequence gave out matching feature points among the six continuous frames of the thoracic continuous temporal image sequence $(0.1 \le t \le 0.6)$ where t is the timestamp of frames in the sequence for all Anatomical Positions (AP) with average translation values. The average translation between inter-frame durations for all common points ‘P’ from the initial to final frame:

$$d_{1avg} = \sum_{p_i=1}^{P} d_1 \Big/ P \quad , \quad d_{2avg} = \sum_{p_i=1}^{P} d_2 \Big/ P \quad \ldots\ldots\ldots\ldots\ldots\ldots \quad d_{N-1avg} = \sum_{p_i=1}^{P} d_{N-1} \Big/ P$$

Below figures (4.4 to 4.6) indicate the image registration process from the sequence for all test subjects through all three APs.

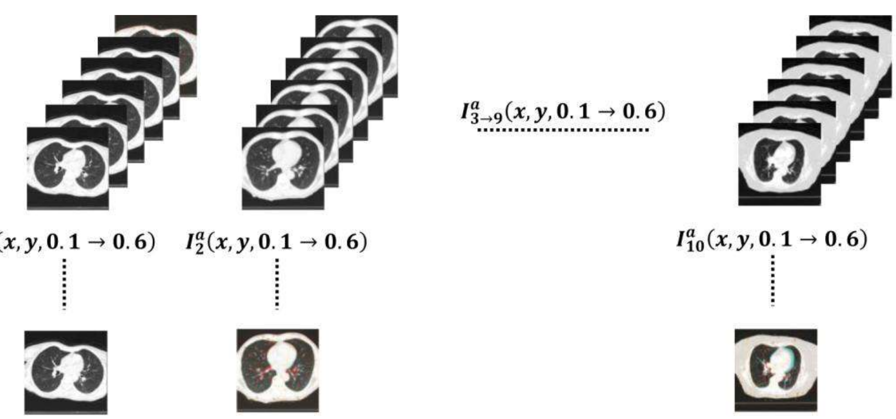

Figure 4.4: Image sequence frames and the registered image for all subjects-Axial

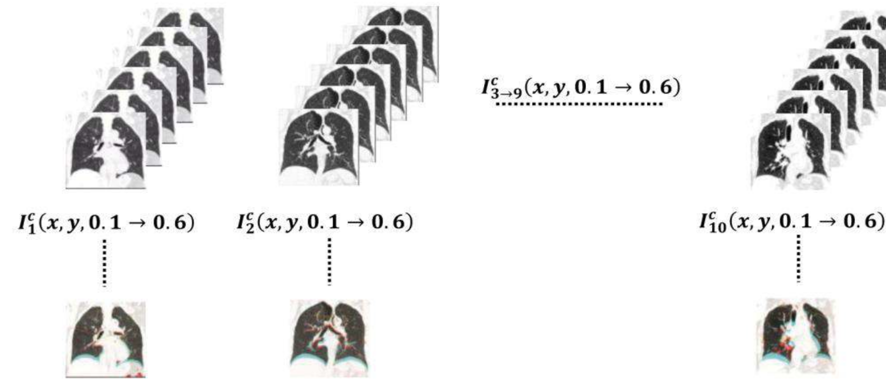

Figure 4.5: Image sequence frames and the registered image for all subjects-Coronal

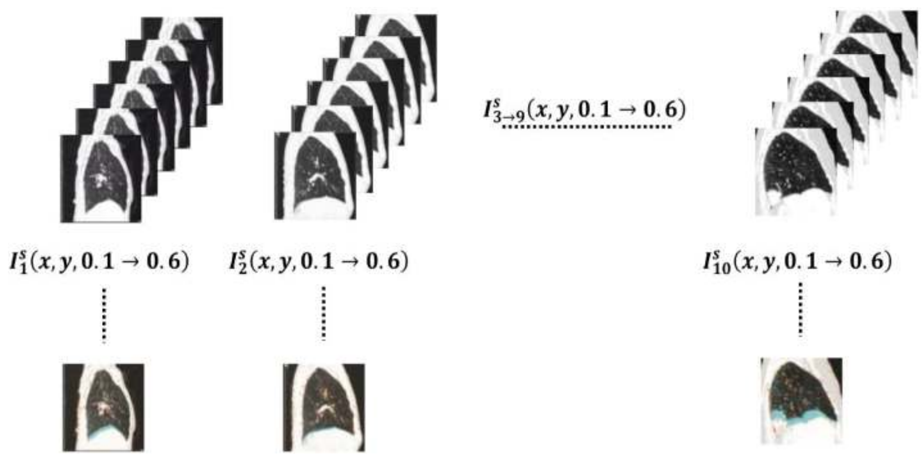

Figure 4.6: Image sequence frames and the registered image for all subjects-Sagittal

Though the proposed method was applied on all the subject data at hand, for representation purposes, subject 'case 5' sagittal AP data has been extensively used (as can be seen in fig. 4.7 to 4.11). The temporal sequence starting from t=0 to t=0.6 s is considered with a gap of 0.1 seconds between two consecutive frames in the sequence. So, frame 1 is the one acquired at t=0.1 and frame 6 is the one corresponding to t=0.6 s.

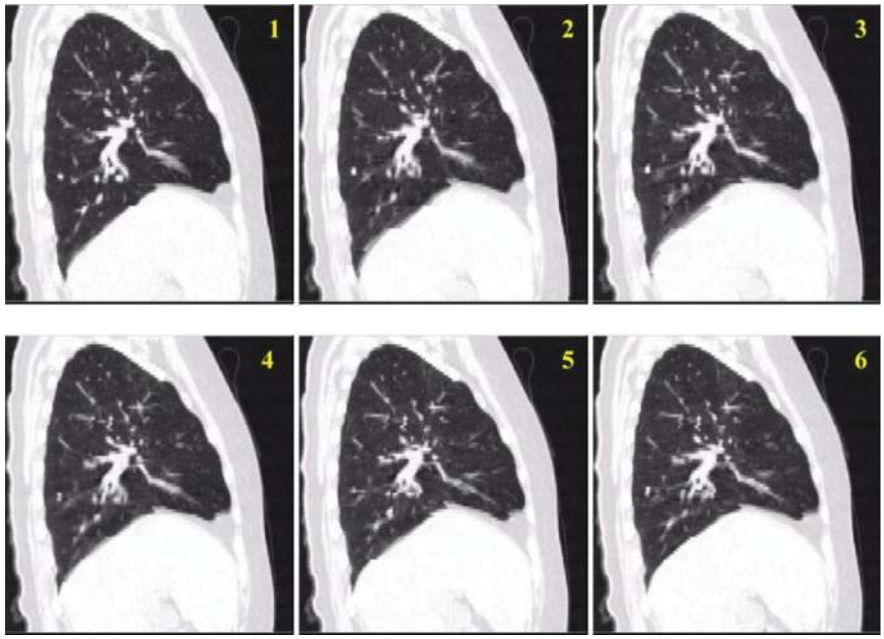

Figure 4.7: The test image temporal sequence (accordingly labelled). Subject 'case 5' Sagittal AP

The feature points are color coded with respect to the indices and IDs assigned to them throughout the process. The trails/tracks they leave after motion also exhibit the same color combination as assigned to respective feature points. There were 242 such feature points for the 'case 5' sagittal AP image sequence, the attributes of which are shown in the table E.1 (Appendix-E). Each of them had a track associated with them; these tracks have been labelled as Track_' point no' where the value of 'point no.' ranges from 0 to 241. Other attributes associated with each track included 'Track_Duration' which indicated the time in seconds for that respective track to finish and the point to reach its ultimate frame. 'Track_Start' is the stating time of every feature point trail/track; the value is '0' for all points, first frame being the reference frame for registration. 'Track_Stop' is the end time in seconds for respective tracks; values may be different for different feature points. 'Track_Displacement' is the net displacement from the point of origin for a feature point over the sequence. 'Track_(X,Y) Locations' are the points of origin of the respective tracks. 'Track_Min/Max/Mean Speeds' are the minimum, maximum and mean speeds of the feature point trail/track for each point through the sequence. The displacement/translation obtained is inherently in pixel units. With the knowledge of PPI (pixel per inch) value of the respective images in question, the displacements can be converted into more tangible units. These average translations for all such feature points for all test subjects through all three APs are shown in tables 4.2 to 4.4. Their corresponding line plots for all 10 subjects are shown as figures 4.12 to 4.14 for easier comparative analysis over the complete breathing pattern. A corresponding false-color registered image representation is shown as fig. 4.9. Optical flow representation of the image sequence with respect to registered image along with a flow orientation scheme is shown in fig. 4.10. The optical flow at any point in the image can be decoded using the flow orientation scheme coding pinwheel given alongside. There was a rather large strip of single color found in the optical flow representation, which is synonymous with the false color representation in fig. 4.9. That is the location with maximum displacement/translation in the sequence and also of maximum deformation with respect to the reference frame.

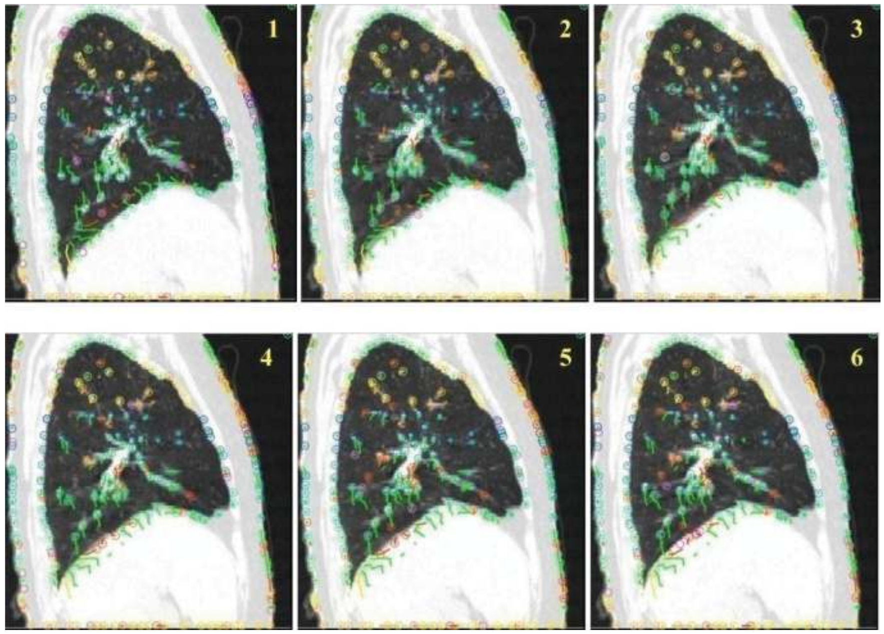

Figure 4.8: The color coded feature points and their colored trails showing the distinct paths for Sagittal AP 'case 5', frames are labeled in order of their temporal sequence

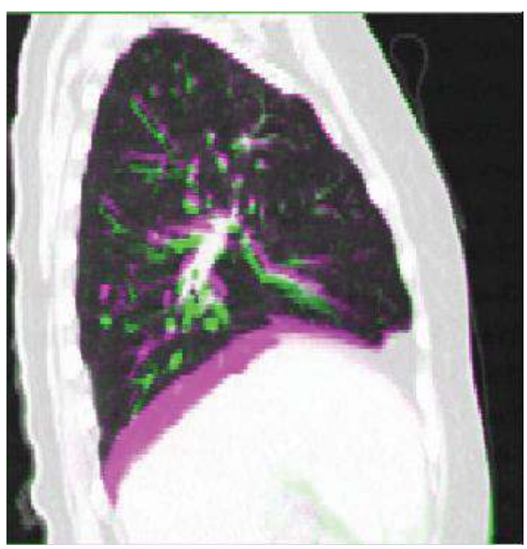

Figure 4.9: The registered image for the corresponding temporal sequence for subject 'case 5' Sagittal AP

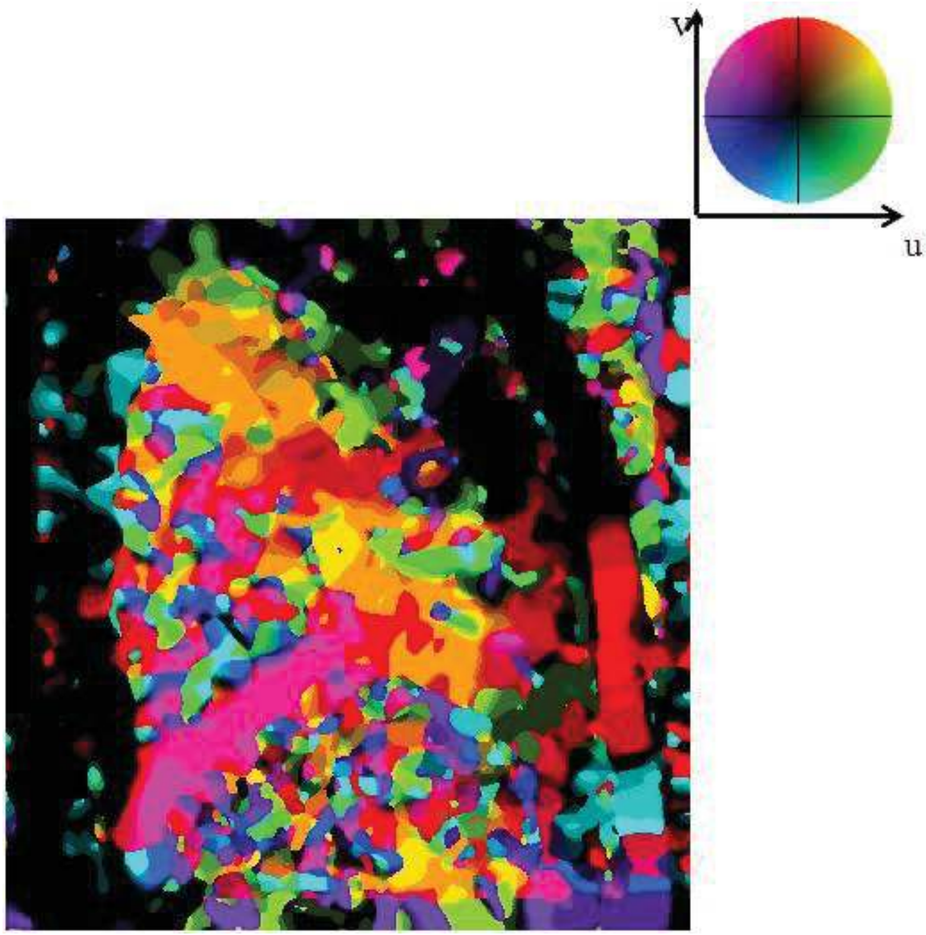

Figure 4.10: Color-coded Optic flow for subject 'case 5' sagittal AP with flow orientation scheme

Where fig. 4.10 indicated the optical flow orientation, magnitude of the optical flow is an important aspect that can be ignored when observing an image sequence over time. Fig. 4.11 represents the optical flow magnitude spread over the complete sequence with the first frame as reference. As can be seen from the magnitude scale provided alongside, the bigger red arrows indicate areas with higher magnitude of flow and larger deformations, while the blue and black arrows indicate areas lower optical flow magnitude and smaller deformations in respective locations.

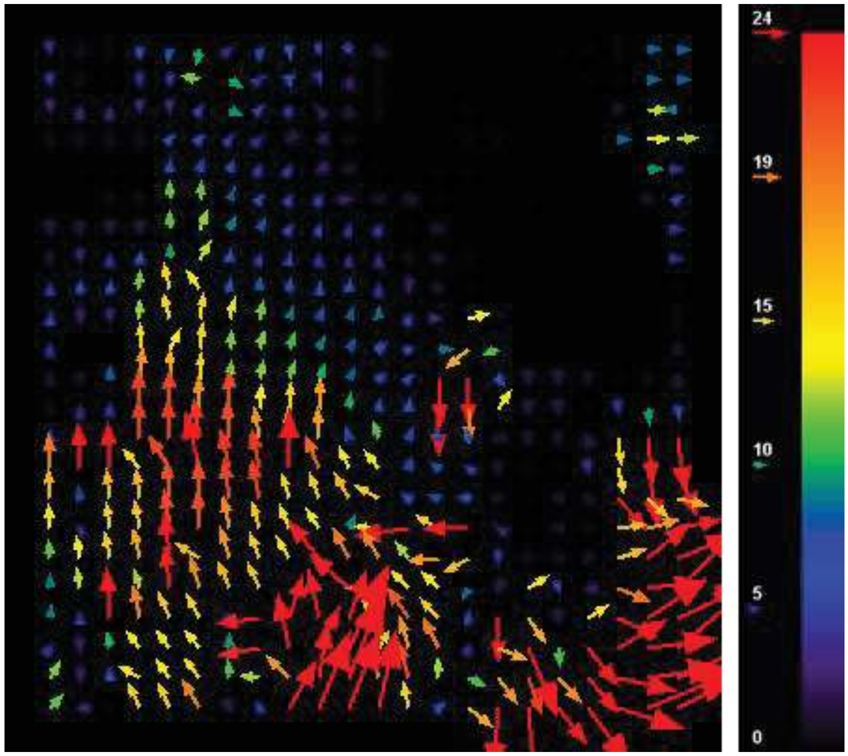

Figure 4.11: The overall image sequence optic flow with magnitude scale

Table 4.2: Average translations (in pixels) for all test subjects through Axial AP

AXIAL Average translation (pixels)										
slices	**case1**	**case2**	**case3**	**case4**	**case5**	**case6**	**case7**	**case8**	**case9**	**case10**
1	0.047	0.000	0.050	0.128	0.103	0.122	0.105	0.081	0.148	0.235
2	0.074	0.054	0.212	0.263	0.220	0.192	0.173	0.176	0.157	0.235
3	0.121	0.090	0.078	0.260	0.217	0.232	0.160	0.197	0.154	0.491
4	0.236	0.041	0.077	0.120	0.335	0.224	0.123	0.236	0.273	0.550
5	0.165	0.087	0.235	0.054	0.229	0.277	0.175	0.227	0.346	0.415

Table 4.3: Average translations (in pixels) for all test subjects through Coronal AP

CORONAL Average translation (pixels)										
slices	**case1**	**case2**	**case3**	**case4**	**case5**	**case6**	**case7**	**case8**	**case9**	**case10**
1	0.049	0.241	0.090	0.337	0.090	0.272	0.413	0.316	0.705	0.389
2	0.257	0.445	0.284	0.441	0.545	0.444	0.574	0.563	1.515	0.587
3	0.544	0.451	0.490	0.436	0.574	0.434	0.547	0.600	1.541	2.594
4	0.555	0.396	0.443	0.414	0.617	0.458	0.522	0.700	1.508	0.707
5	0.361	0.381	0.529	0.495	0.682	0.532	0.503	0.645	1.432	0.586

Table 4.4: Average translations (in pixels) for all test subjects through Sagittal AP

SAGITTAL Average translation (pixels)										
slices	**case1**	**case2**	**case3**	**case4**	**case5**	**case6**	**case7**	**case8**	**case9**	**case10**
1	0.056	0.102	0.033	0.198	0.022	0.218	0.283	0.387	0.318	0.348
2	0.067	0.038	0.031	0.225	0.081	0.515	0.451	0.603	0.410	0.439
3	0.229	0.144	0.036	0.184	0.131	0.511	0.504	0.639	0.336	0.476
4	0.120	0.125	0.041	0.228	0.092	0.483	0.574	0.666	0.374	0.521
5	0.131	0.042	0.027	0.237	0.079	0.545	0.504	0.659	0.326	0.505

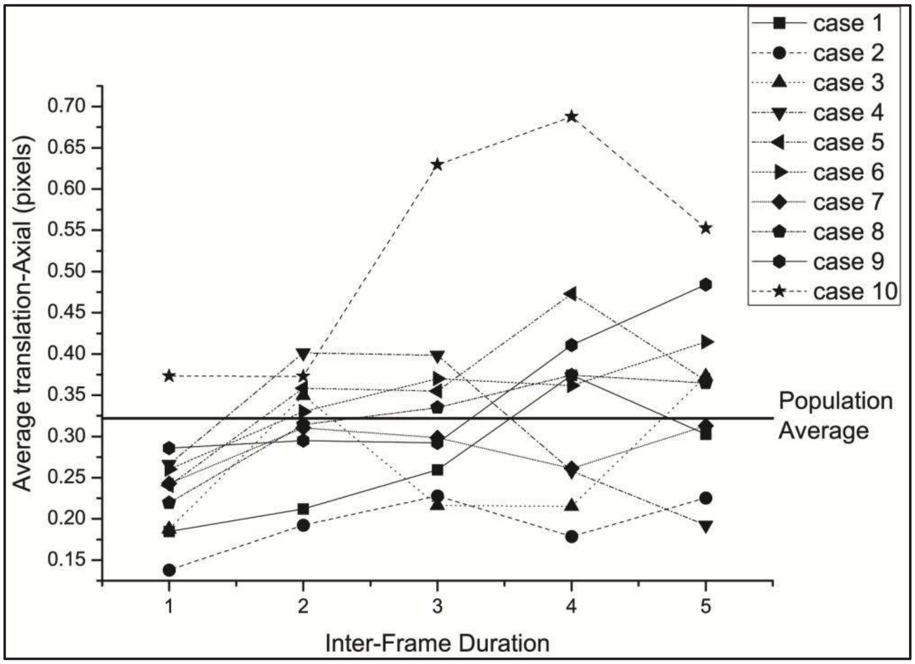

Figure 4.12: Average displacement for all subjects in Axial AP

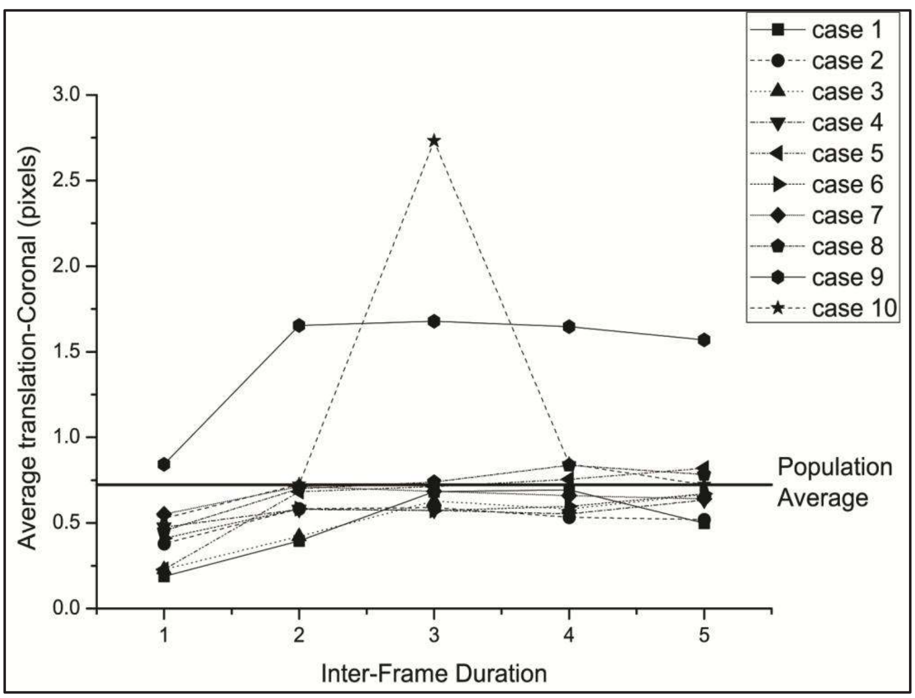

Figure 4.13: Average displacement for all subjects in Coronal AP

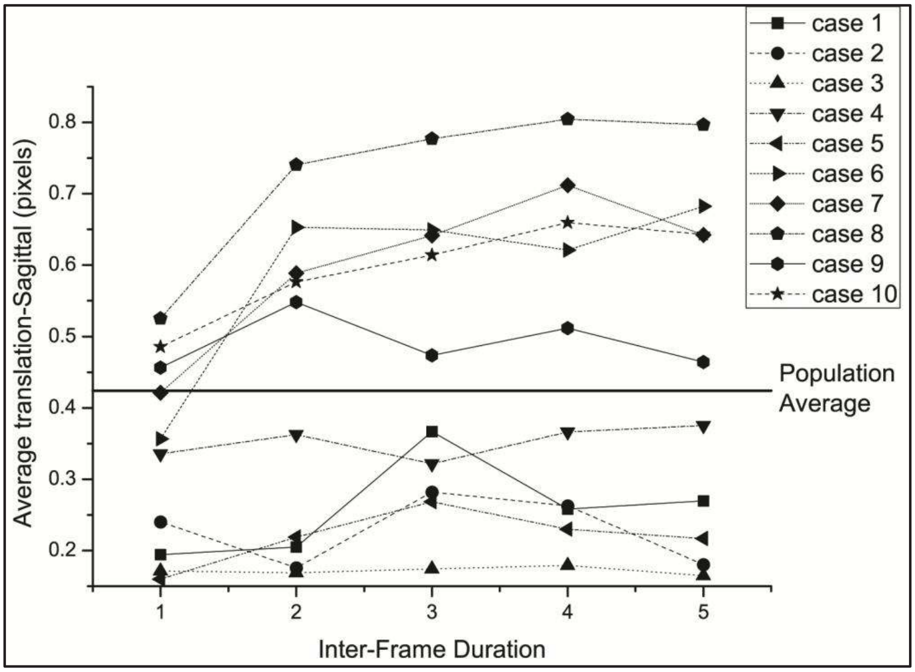

Figure 4.14: Average displacement for all subjects in Sagittal AP

As we can see in fig. 4.12, the axial translations were recorded highest for subject 'case 10' and the lowest corresponding values were for 'case 2'. The average value for 'case 10' was recorded at 0.3851 pixels, which was way above the population average of 0.184 shown by a line across the plot. In case of coronal AP as can be seen in fig. 4.13, the biggest deformations throughout the sequence are exhibited by the subjects 'case 10' and 'case 9' at 2.594 and 1.54 pixels respectively. The population average in this case being 0.5847 marked by a straight line in the corresponding plot. Though apart from 'case 10' only 'case 9'exhibited bigger deviations than the average value, the change in deformation with respect to inter-frame durations was more or less constant; on the other hand 'case 10' exhibited enormous shift from the average value while transitioning from 3rd frame to 4th frame. Looking at fig. 4.14 for the sagittal AP, all subjects though a bit above and below the average maintain an almost constant rate of change in the deformations and do not exactly exhibit any erratic patterns through the observed full inhale to exhale process. After having a comprehensive look at all subjects' deformation pattern data through axial, coronal and sagittal APs collectively, it was inferred that subject 'case 10' singled out as the only one with maximum deformation. This analysis indicates anomalous breathing patterns from the aforementioned subject among the considered consensus average.

4.5 Conclusion

A framework has been presented showing how to use a feature point set generated using a Hessian-matrix based feature detector and Haar wavelets based descriptor such as SURF through a motion estimation technique such as OFM tracking for deformable image transformations in medical images such as the thoracic 'pectus excavatum' [Haller, J. A. et al., 1987; Kim, H. C. et al., 2010] full exhale and full inhale used in this work. This conclusion is of high clinical relevance from a diagnostic point of view as well; the artifacts and position uncertainties due to uneven breathing patterns which hamper the image guided clinical interventions can be corrected to a point where there influence on the actual data and the diagnostics based on them is brought down to the least.

This work can be looked upon as an automatic way of deformable image registration for high contrast medical images using landmark (control) points. Although the proposed methodology provides with a fast and accurate way of DIR for medical images and thus an account of deformity in the thoracic periphery, there is much scope for improvement in the overall process. One way this can be achieved in future is by modifying the SURF and/or the Motion estimation procedure involved in the process. Another way is to improve and enhance the quality as well as the quantity of the database used. Also, the aforementioned procedure can provide better results if applied for a different human anatomy altogether.

However diligently and accurately it may have been done, there might still be some scope of improvement and betterment in the methodology and also in its presentation. The search and pursuit of better methods for deformable medical image registration is still on.

Chapter 5: Deformable Thoracic CT Images Sequence Registration using Strain Energy Minimization

The idea of deformable image registration (DIR) has been explored for a thoracic CT (computed tomography) image database of ten subjects. Thoracic CT image acquisition for clinical interventions requires a well-defined procedure which has already been underlined on the basis of field expertise and past experiences. Despite strict adherence to the procedure, the acquired images are prone to distortions and artefacts. This might happen due to organ motion during breathing process (at times even in breath-hold procedures), slight (even involuntary) movements or acquisition variations in supine and prone positions etc. An intensity differences based energy minimization method has been proposed. The moving image is transformed in the process such that it gets maximum alignment with the fixed image. This is achieved by energy minimization of the moving image in an iterative process. It is a simpler and more practical method for thoracic CT image registration than the prevalent approaches. This has been shown by lower mean registration errors for the patient data; the errors were as such axial: 0.283±0.08, coronal: 0.784±0.32 & sagittal: 0.66±0.2 pixels. This registration of moving image onto the fixed image in the sequence will help in minimizing the adverse effects of the otherwise present discrepancies, phase errors and discontinuity artifacts that might have crept in during the acquisition.

The proposed method begins with a pair of images of same dimensions; these images are part of an image sequence and have considerable temporal difference between them. The image sequence has been acquired as a part of the breathing process. Of the two, image appearing earlier in the temporal timeline is considered as the target image and the one appearing later is considered as the source image. These both images represent the extremes of a breathing cycle such that the first image is full inhale and the last image is full exhale. These both images have their own specific energy signatures. Both these images have to be registered against each other. For the registration process, no direct comparisons between images are done; instead the source image is independently transformed in such a way that the transformed image has minimum intensity difference with the target image. It is an iterative process (as can be referred to in fig. 5.2), at each stage of which transformed versions of source image are compared to the target image for intensity difference of zero or less than a third decimal place value. If none of the two conditions are met, the transformed image goes into further transformation and the process continues until the source image is transformed to a level that it satisfies previously laid conditions. In our experiments, SNR (signal to noise ratio), PSNR (peak SNR), mean SSIM (Structural SIMilarity) index & NCC (Normalized Cross Correlation) have been used to estimate and establish increased similarity between the later transformed – target image pair in comparison to previous source – target image pair. Mean Registration Error (E_{T-R}) is used as the quantitative measure for the evaluation of performance. The E_{T-R} obtained for the dataset was found to be considerably lower than more traditional and prevalent transforms such as affine and b-splines based approaches.

5.1 Introduction

Organ motion pertaining to breathing can lead to image artefacts and position uncertainties during image guided clinical interventions. A particular case for such image guided interventions (IGI) can be the radiotherapy planning of thoracic and abdominal tumours; the respiratory motion causes important uncertainties and is a significant source of error [Keall, P. J. *et al.*, 2006]. During a process of image acquisition, slight movement from the subject can translate into potential discrepancies in the acquired image sequence. Images in such an acquired sequence more than often end up out of sync and prove to be not of much use for both medical application and/or research purposes. A non-invasive method to describe lung deformations was proposed using NURBS surfaces based on imaging data from CT scans of actual patients [Tsui, B. M. W. *et al.*, 2000]. Image registration has recently started playing an important role in this scenario; it helps in the estimation of any motion caused due to breathing during acquisition and the description of the temporal change in position and shape of the structures of interest by establishing the correspondence between images acquired at different phases of the breathing cycle [Ehrhardt, J. *et al.*, 2011].

Image Registration is the alignment/overlaying of two or more images so that the best superimposition can be achieved. These images can be of the same subject at different points in time, from different viewpoints or by different sensors. This way the contents from all the images in question can be integrated to provide richer information. It helps in understanding and thus reducing the differences occurred due to variable imaging conditions. Most common applications of Image Registration include remote sensing (integrating information for GIS), combining data obtained from a variety of imaging modalities (combining a CT and an MRI view of the same patient) to get more information about the disease at once, cartography, image restoration etc. An image registration method targets to find the optimal transformation that aligns the images in the best way possible. Image registration methods can be broadly classified into three basic classes, landmark (or point) based registration [Mcgregor, B., 1998; Rohr, K. *et al.*, 2001; Bookstein, F. L., & Green, W. D., 1993], segmentation based registration [Sull, S., & Ahuja, N., 1995; Feldmar, J., & Ayache, N., 1996; Jain, A. K. *et al.*, 1996] and the image intensity based registration [Szeliski, R., & Coughlan, J., 1994; Kybic, J., & Unser, M., 2003] depending on them being more cost efficient, fast and flexible over the others with respect to the image family it is being used to register and the application of the registration process. It is further categorized into two kinds based on the type of image it is being applied for. The two kinds of images are Rigid Images and Deformable Images. Rigid images are those of structures with rigid morphological properties e.g. bones, buildings, geographical structures etc. If the underlying transformation model allows local deformations, i.e. nonlinear fields' u(x), then it is called Deformable Image Registration (DIR) [Muenzing, S. E. A. *et al.*, 2014]. Deformable images are those of structures shape and size of which can be modelled after tangible physically deformable models [Sotiras, A. *et al.*, 2013]. Rigid image registration although is an important aspect of registration it is not the topic of discussion in this article. Since the discussion is about Medical Image Registration and almost all anatomical parts or organs of the human body are deformable structures, the concentration here is on DIR [Oliviera, F. P. M. & Tavares, J. M. R. S., 2012].

The proposed methodology is based on intensity based registration. It is fully automatic in its mode of operation and helps in faster and more accurate image registration in comparison to pure landmark based registration methods. This factor gives our method an upper hand when it comes to real-life medical image registration problems. The intensity based energy minimization methodology seems more practical, stable and cost efficient for deformable images in comparison to landmark based or segmentation based methodologies for similar purposes. The method is simpler and faster than its contemporaries because the energy function is worked upon directly without solving large matrix system assemblies.

5.2 Background

The background study of this chapter initially includes a study of few most prominent proposed algorithms in the direction of study of the energy minimization based non-linear elastic image registration and its applications. Then the proposed methods relating to image registration of thoracic CT images are discussed. The propositions are categorically discussed keeping in mind their acute relevance and their year of occurrence. Propositions occurring at a later instant in timeline are given higher priority in terms of detailed discussion in comparison to earlier works to establish better context. These methods are compared in a tabular format in table D.1 in Appendix D.

Pennec and associates [Pennec, X. *et al.*, 2005] suggested a statistical regularization framework for non-linear registration based on the concept of Riemannian Elasticity. In the proposed method, elastic energy has been interpreted as the distance of the Green-St. Venant strain tensor to the identity, which in turn reflects the deviation of the local deformation from a rigid transformation. By changing the usually employed Euclidean metric for a more suitable Riemannian one, a consistent statistical framework has been defined to quantify the amount of deformation. These statistics were then used as parameters in a Mahalanobis distance to measure the statistical deviation from the observed variability, giving a new regularization criterion that is called the statistical Riemannian elasticity. It was found that this new criterion is able to handle anisotropic deformations and is inverse-consistent. Preliminary results and observations showed that it can be quite easily implemented in a non-rigid registration algorithm.

Bao Zhang and associates [Zhang, B. *et al.*, 2011] proposed a three-dimensional elastic image registration methodology based on strain energy minimization with its application to prostate magnetic resonance imaging. The registration algorithm was also applied on ten sets of human prostate data, each with two typical deformation states (one with 0 cc of air and the other with 40–60 cc of air inflated in the endorectal coil balloon). There were a total of 200-400 landmarks used to derive the transformation depending on the size of each prostate. They described it as a novel 3-D elastic registration procedure that is based on the minimization of a physically motivated strain energy function that requires the identification of similar features (points, curves, or surfaces) in the source and target images. The Gauss-Seidel method was used in the numerical implementation of the registration algorithm. The registration procedure was validated on synthetic digital images, MR images from prostate phantom, and MR images obtained on patients. Registration errors were assessed by averaging the displacement of a fiducial landmark in the target to its corresponding point in the registered image. The registration error on patient data was 1.8±0.7 pixels. Registration also improved image similarity (normalized cross-correlation) from 0.72±0.10 to 0.96±0.03 on patient data. Registration results on prostate data in vivo demonstrated that the registration procedure could be used to significantly improve both the accuracy of localized therapies such as brachytherapy or external beam therapy and can be valuable in the longitudinal follow-up of patients after therapy.

Ronald W. K. So and associates [So, R. W. K. *et al.*, 2011] proposed a technique for non-rigid image registration of brain magnetic resonance images using graph-cuts. A graph-cut based method was proposed for non-rigid medical image registration on brain magnetic resonance images. In this proposal the non-rigid medical image registration problem has been reformulated as a discrete labelling problem. They modelled the non-rigid registration as a multi-labeling problem by Markov random field. The image registration problem was therefore modeled by two energy terms based on intensity similarity and smoothness of the displacement field. The MRF energy was minimized using graph-cuts algorithm via α-expansions. The registration results of the proposed method were compared with two state-of-the-art medical image registration approaches: free-form deformation based method and demons method. In addition, the registration results were also compared with that of the linear programming based image registration method. The proposed method was found to be more robust against different challenging non-rigid registration cases with consistently higher registration accuracy than those three methods, and gives realistic recovered deformation fields.

Andrew R. Dykstra and associates [Dykstra, A. R. *et al.*, 2012] proposed a method which co-registers high-resolution preoperative MRI with postoperative computerized tomography (CT) for the purpose of individualized functional mapping of both normal and pathological (e.g., interictal discharges and seizures) brain activity. The proposed method accurately (within 3 mm, on average) localizes electrodes with respect to an individual's neuroanatomy. Furthermore, they outlined a principled procedure for either volumetric or surface-based group analyses. The method was demonstrated in five patients' data with medically-intractable epilepsy undergoing invasive monitoring of the seizure focus prior to its surgical removal. Accuracy of the method was found within 3mm of average. The straight-forward application of this procedure to all types of intracranial electrodes, robustness to deformations in both skull and brain, and the ability to compare electrode locations across groups of patients makes this procedure an important tool for basic scientists as well as clinicians.

H. P. Heinrich and associates [Heinrich, H. P. *et al.*, 2013] proposed a MRF-Based Deformable Registration and Ventilation Estimation of Lung CT. In the proposed method three major challenges associated with lung ct registration viz. large motion of small features, sliding motions between organs and changing image contrast due to compression are addressed and potentially higher quality of discrete approaches is preserved. First, an image-derived minimum spanning tree is used as a simplified graph structure, which coped well with the complex sliding motion and allowed to find the global optimum very efficiently. Second, a stochastic sampling approach for the similarity cost between images is introduced within a symmetric, diffeomorphic B-spline transformation model with diffusion regularization. The complexity is reduced by orders of magnitude and enables the minimization of much larger label spaces. In addition to the geometric transform labels, hyper-labels are introduced, which represent local intensity variations in this task, and allow for the direct estimation of lung ventilation. The improvements are validated in accuracy and performance on exhale-inhale CT volume pairs using a large number of expert landmarks. The three challenges posed in the beginning are met.

Keita Nakagomi and associates [Nakagomi, K. *et al.*, 2013] proposed a segmentation based registration methodology which uses multi-shape graph cuts with neighbour prior constraints for lung segmentation from a chest CT volume. A novel graph cut algorithm has been proposed that can take into account multi-shape constraints with neighbor prior constraints, and reports on a lung segmentation process from a three-dimensional computed tomography (CT) image based on this algorithm. It is a novel segmentation algorithm that improves lung segmentation for cases in which the lung has a unique shape and pathologies such as pleural effusion by incorporating multiple shapes and prior information on neighbour structures in a graph cut framework. The efficacy of the proposed algorithm is demonstrated by comparing it to conventional one using a synthetic image and clinical thoracic CT volumes.

5.3 Method

5.3.1 Preparation

The dataset used comprised of a total (3×10)×10 i.e. 300 thoracic CT images across 10 subjects. All images were anonymized and all procedures followed were in accordance with the ethical standards of the responsible committee on human experimentation (institutional and national) and with the Declaration of Helsinki 1975, as revised in 2008 (5). Informed consent was obtained from all patients for being included in the study. All patients or legal representatives signed informed consent. The images lie between CT phases 0-5 i.e. end-inspiration to end-expiration in timestamp range t00→t05. The image dimensions lie between 396×396 to 432×400 pixels. There were 6 frames from a temporal thoracic image sequence each for every Anatomical Plane (AP) i.e. Axial (supine), Coronal and Sagittal for all the 10 subjects acquired simultaneously with a gap of 0.1 second starting from time t= 0.1 to 0.6 seconds. All images were identified as $I_N^{AP}(x, y, t)$ where $\{N, t \in \mathbb{R}^+ | 1 \leq N \leq 10, 0.1 \leq t \leq 0.6\}$, (x, y) are the x & y coordinates in the Cartesian plane and AP signifies the three anatomical planes of view i.e. Axial (a), Coronal (c) and Sagittal (s). Suppose the 3rd frame from coronal AP for subject 'case 9', would be notified as $I_9^c(x, y, 0.3)$. A view of the image database is shown in the table 5.1 for representational purposes.

Table 5.1: All three anatomical viewpoints for all the 10 subjects at time t=0.1 & 0.6 sec

	ANATOMICAL PLANES (T & S Images)		
	Axial	**Coronal**	**Sagittal**
1	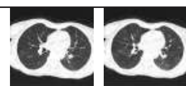	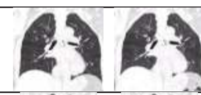	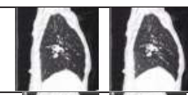
2	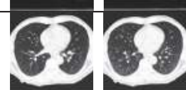		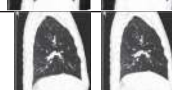
3	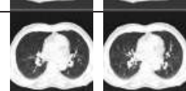		
4	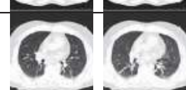	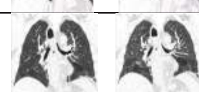	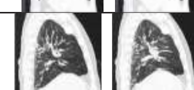
5	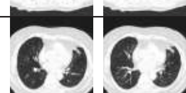		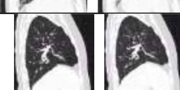
6	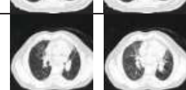	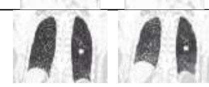	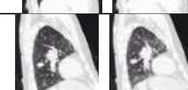
7	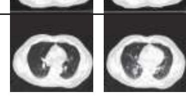		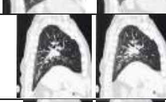
8	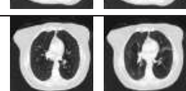		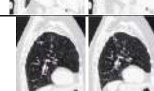
9	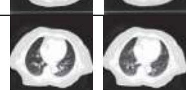		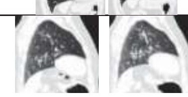
10	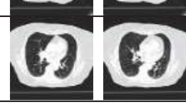		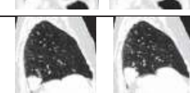

5.3.2 Proposed Methodology

What we have is a temporal sequence of images starting from time t=0.1 to t=0.6 seconds. It starts from the end- inspiration phase and continues up to the end-expiration phase of the breathing cycle. The last image of the aforementioned sequence being diametrically most deformed with respect to the first image. We have proposed a method to register these two images with respect to each other. The two images are the target (T) and the source images (S) at t=0.1 and t=0.6 sec. respectively. These images belong to the same domain Ω and are related through a transformation $\mathrm{T_R}$. This transformation is such that the resulting transformed image (S') has the minimum energy distribution difference in terms of a similarity measure with the target image T, this has been shown in fig. 5.1. In simpler terms it can be stated as: 'a transformation sought such that the transformed image has minimum intensity difference with the target image'.

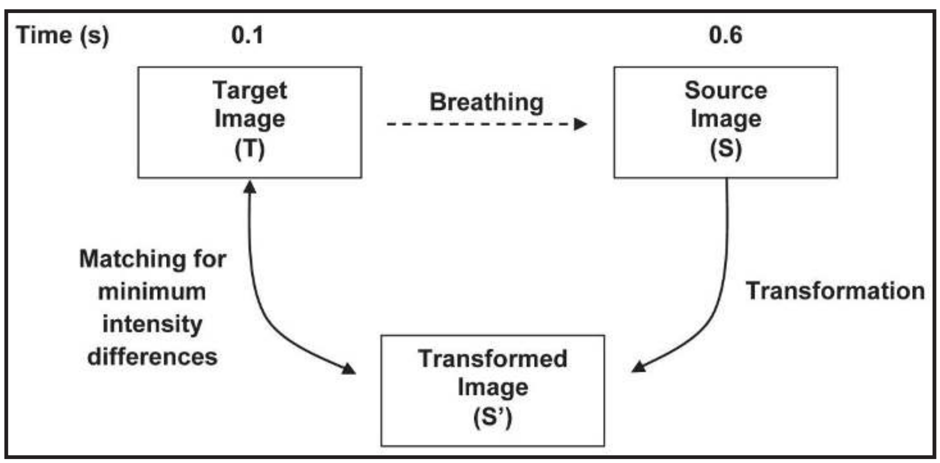

Figure 5.1: Overview of the proposed methodology

There is a potential energy associated with an elastic system at a time. Since, the images involved in the study are of a human body organ, they can be categorized as non-rigid or deformable images and the energy principles of elastic systems are applicable to this set of images. Potential energy of an elastic two dimensional system at static equilibrium is pure strain energy; it can be defined as [Ugural, A. C., & Fenster, S. K., 2003]:

$$U = \iint_{\Omega} {}^{1}/_{2}\left[\lambda e^{2} + 2\mu\left(\varepsilon_x^2 + \varepsilon_y^2\right) + \mu\gamma_{xy}^2\right] d\Omega \tag{5.1}$$

where Ω is the image dimension, λ is the tensile stress (engineering constant), μ is the shear modulus, together they are called the Lame' constants; ε_x and ε_y are normal strains in the x and y directions respectively, γ_{xy} is the shear strain in the x-y plane pointing towards the y direction and 'e' is the unit change in image dimensions.

The Poisson's ratio value for Lung tissue averages close to 0.46 [Al-Mayah, A. et al., 2008; Brock, K. K. et al., 2005; Sundaram, T. A., & Gee, J. C., 2005, Zhang, T. et al., 2004]. In equation 5.1, the first term 'λe^2' can be ignored since it is two order lower than the rest of the terms. This makes the energy expression independent of tensile stress λ:

$$U = \iint_{\Omega} {}^{1}/_{2}\left[2\mu\left(\varepsilon_x^2 + \varepsilon_y^2\right) + \mu\gamma_{xy}^2\right] d\Omega$$

this can be further simplified to:

$$U = \mu \iint_{\Omega} \left[\left(\varepsilon_x^2 + \varepsilon_y^2\right) + {}^{1}/_{2}\,\gamma_{xy}^2\right] d\Omega \tag{5.2}$$

Suppose u, v are the displacements in x and y directions respectively. Normal strain ε_a is defined as $\frac{extension}{original\ \ lengt\,h}$ in the direction 'a' (a= x, y); shear strain γ_{ab} in the plane a-b would be the sum of angle of shear (for smaller degrees of shear). Thus, $\varepsilon_x = \frac{\partial u}{\partial x}$ and $\varepsilon_y = \frac{\partial v}{\partial y}$, similarly $\gamma_{xy} = \frac{\partial u}{\partial y} + \frac{\partial v}{\partial x}$. Exacting these values to equation 5.2:

$$U = \mu \iint \left[\left({}^{\partial u}/_{\partial x}\right)^2 + \left({}^{\partial v}/_{\partial y}\right)^2\right] dxdy + {}^{1}/_{2}\,\mu \iint \left[\left({}^{\partial u}/_{\partial y} + {}^{\partial v}/_{\partial x}\right)^2\right] dxdy \tag{5.3}$$

So, the expression for energy function 'U' in equation 5.1 has been reduced to strictly a strain energy function in equation 5.3, the equation 5.3 hence can be rewritten for U_{strain} as:

$$U_{strain} = \mu \iint \left[\left({}^{\partial u}/_{\partial x} \right)^2 + \left({}^{\partial v}/_{\partial y} \right)^2 \right] dxdy + {}^{1}/_{2}\, \mu \iint \left[\left({}^{\partial u}/_{\partial y} + {}^{\partial v}/_{\partial x} \right)^2 \right] dxdy \qquad (5.4)$$

The strain energy 'U_{strain}' minimization requires that over the image boundary conditions between the source and the target images:

$$\delta U_{strain} = 0 \qquad (5.5)$$

Such that the minimization constraint can be expressed in terms of intensity difference between the transformed image (S') and the target image (T) over the image dimensions' (Ω) as:

$$\int_{\Omega} (I_{S'} - I_T)\ \mathrm{d}\Omega = 0 \qquad (5.6)$$

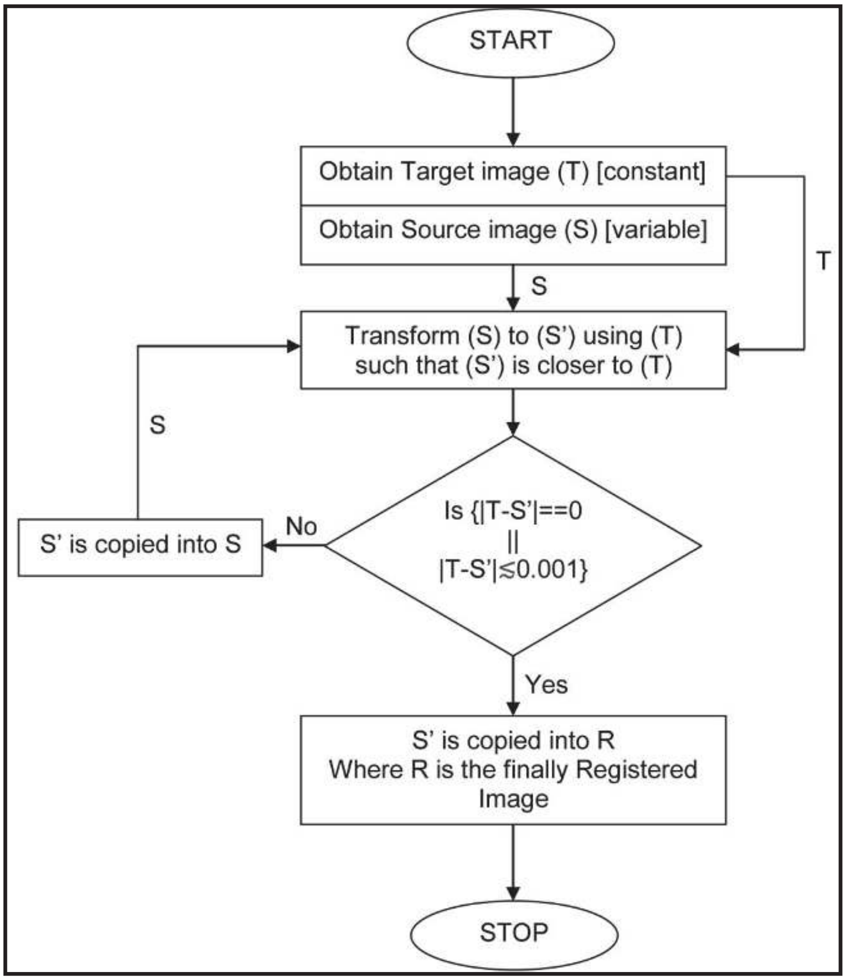

Figure 5.2: Flowchart of the iterative process in the registration procedure

It is an iterative process; as we can see in the fig 5.2, during the iteration, each time a transformed image is obtained, it is compared against the fixed image and an intensity difference mapping and value is calculated. These intensity differences are checked at each step. If very little or negligible change (say up to third decimal place) is observed, the iteration is stopped and the finally transformed image is considered as the required registered image. In case of progressively changing intensity differences for consecutive iterations, the iteration is continued until the stopping factor comes into play.

5.4 Results and Discussion

Iterative energy minimization using intensity differences across the image boundaries yield a transformed image (S') which was pitted against the actual target image (T) at different stages of the iteration to assess the level of transformation. Out of the ten subjects' data at hand, the coronal AP of subject 'case 3' has been chosen to elaborate and demonstrate the proposed technique with results. The transformed image (S') after the complete registration process showed an increase of 51.64% SNR (signal-to-noise ratio) value with respect to the target image (T) in comparison to the source image (S) with respect to target image. The change in PSNR (peak SNR) value was recorded at 41.64% in S'-T in comparison to S-T pair. A new metric called the SSIM (Structural Similarity) index has been used [Wang, Z. et al., 2004]. It has been used to estimate and measure the similarity between two images. It has been used as a deciding metric which would give a percentage similarity between the two images in question i.e. the fixed and the moving image and the fixed-transformed image pair. The mean SSIM index for the S-T pair was calculated at 0.4975, the same index for the S'-T pair came at 0.735. Along with similarity measures such as SNR, PSNR and m-SSIM, NCC (normalized cross-correlation) has been used to demonstrate as to how close the transformed image (S') has come to the target image (T) as a result of the registration process. The NCC value for S-T pair was estimated at 0.8817, for the S'-T pair it was calculated at a higher value of 0.9749 which further helps in establishing the closeness of the transformed image to the target source and hence, the proposed methodology as an efficient deformable image registration approach.

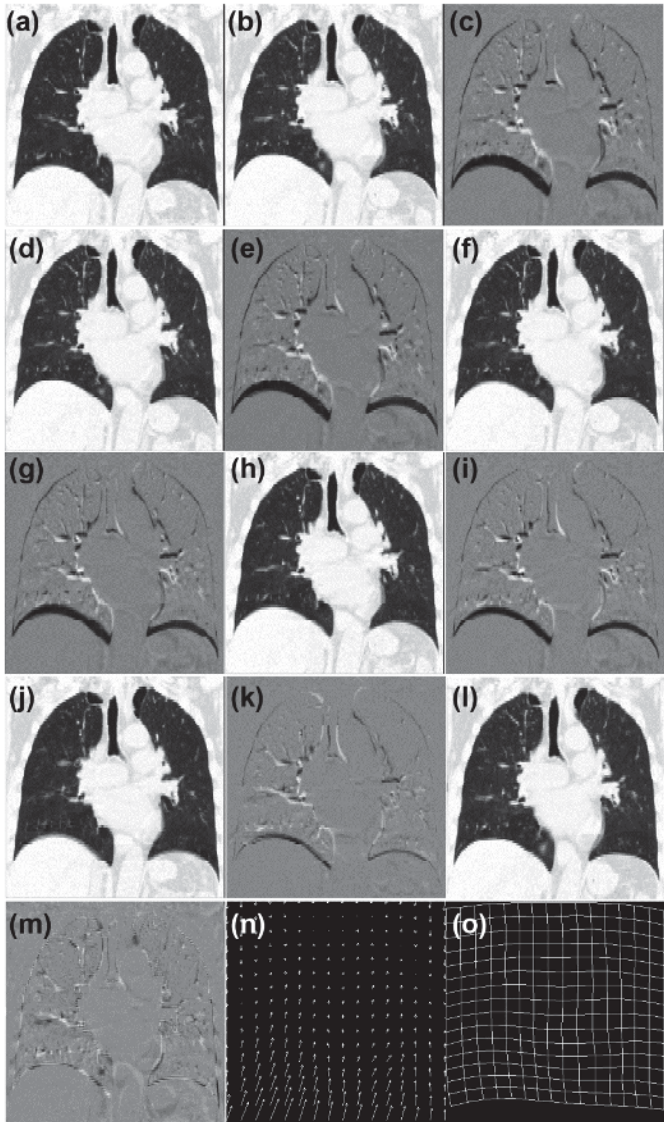

Figure 5.3: The iterative process graphical results on 'case 3' coronal AP

The earlier discussed iterative process and how it results in the finally registered image has been shown in the fig. 5.3. Figure 5.3(a) & (b) are the fixed and moving images respectively, they are also the diametrically opposite images of a breathing cycle (i.e. full inhale and full exhale) in a respiration process. Figure 5.3(c) is the intensity difference mapping (IDM) of (a) & (b) before the iteration starts. Transformation is applied to the moving image and transformed image is obtained. An IDM and corresponding value is calculated for the newly transformed moving image and the fixed image. Changes in IDM and value for current and previous stage is observed, if the change is zero or negligible in comparison to the intensity difference value at either of the two stages of the iteration, the iteration is stopped there and last transformed image is the registered image. Figure 5.3(d) is the transformed image at the 7th iteration, 5.3(e) is its IDM with respect to the fixed image. In this particular instance of subject ‘case 3’, it took 174 iterations to obtain the finally registered image which is the fig. 5.3(l); 5.3(m) is the final IDM indicating minimal difference of the registered image with respect to the fixed image indicating a seamless and smooth registration process. Figures 5.3(f) and (g) are the transformed and IDM (with the fixed image) images at 20th iteration; figs. 5.3(h) and (i) are the transformed and IDM (with the fixed image) at the 55th iteration; similarly 5.3(j) and (k) are the same at the 130th iteration. Figure 5.3(n) and (o) are the deformation vector and deformation field representations respectively for the finally registered image.

Figure 5.4 shows the energy minimization process for subject ‘case 3’ coronal AP, the iterative process continues until a finally registered image is obtained at 174th iteration (that is where the minimization process stops). The initial descent was observed as fast with respect to iterations until 110th iteration, after which the minimization process progresses with diminutive changes in intensity differences. It finally picks up at 124th iteration until to finally finish the process at 174th.

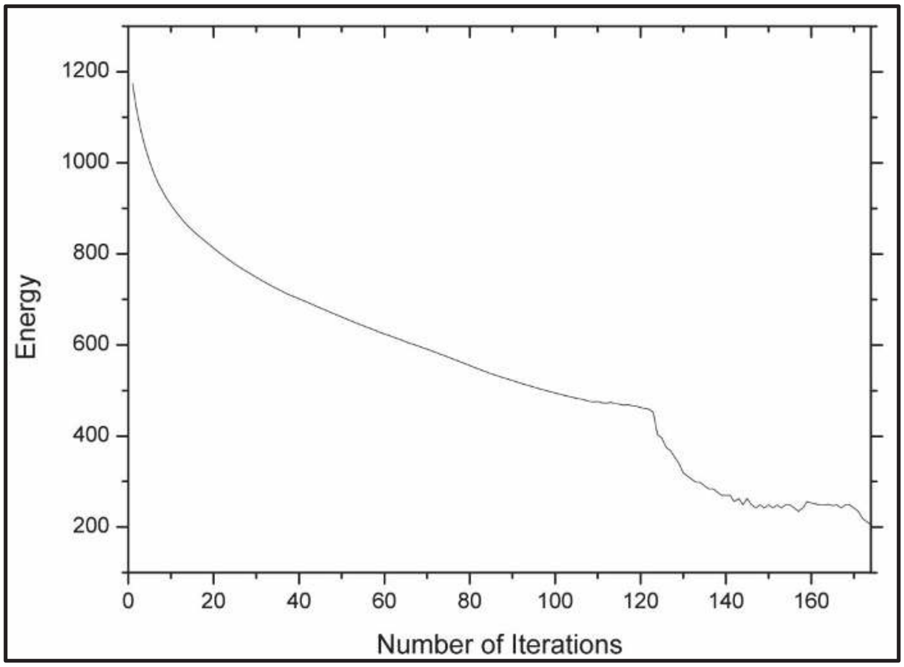

Figure 5.4: Energy minimization vs. Iterations for 'case 3' coronal AP

Table 5.2: SNR, pSNR, m-SSIM, NCC for all subjects under study from all APs; S-T is the source-target pair, R-T is registered-target pair for proposed method

Similarity estimation of S-T and R-T using various metrics for all subjects						
	Axial		**Coronal**		**Sagittal**	
	S-T	**R-T**	**S-T**	**R-T**	**S-T**	**R-T**
SNR (dB)	16.23±1.48	16.29±1.96	12.51±1.37	16.29±1.62	12.62±1.3	16.13±1.6
PSNR (dB)	20.52±1.14	20.58±1.62	15.35±1.36	19.13±1.6	16.33±1.5	19.83±1.8
m-SSIM index	0.744±0.05	0.742±0.04	0.49±0.08	0.58±0.12	0.57±0.13	0.64±0.14
NCC	0.964±0.01	0.969±0.01	0.85±0.03	0.93±0.02	0.89±0.03	0.95±0.03

The proposed technique was practically implemented on all the subject data at hand i.e. three anatomical positions across ten subjects. After obtaining the finally registered images for complete dataset, they were pitted against the fixed images of their own sequence's respective sub-datasets. Similarity metrics such as SNR, pSNR, mean-SMIM index and NCC were calculated and compared for each S-T and R-T pairs for improvements (if any) which might suggest closeness of the registered image towards the fixed image. The observations are collected in table 2, they are average values over the complete dataset through all APs; all similarity metrics clearly seem to improve from S-T to R-T image pair for all subjects. Where there are significant changes in the case of coronal and sagittal APs, respective changes are not as notable in axial AP's data, this can be explained by usually comparatively smaller deformations in the 'anterior-posterior' direction.

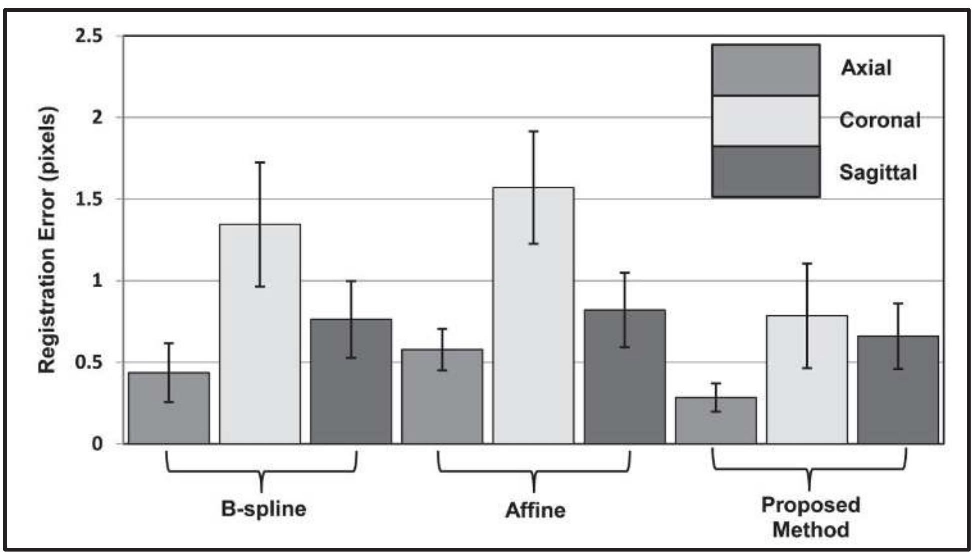

Figure 5.5: mean Registration error (pixels) for all 10 subjects through all APs

As can be seen in the figure 5.5, the mean registration errors (E_{T-R}) obtained for all the subjects involved in the test have been plotted through all three APs. Without the scope of any significant deformations comparable with coronal and sagittal APs, lowest mean registration errors were recorded for axial APs after using all the tested transforms. The proposed method yielded least mean E_{T-R} (for all APs) while followed by b-spline and affine transforms in order. Not relying on landmark based features to establish correspondences instead applying purely intensity difference based energy minimization can be attributed for these results.

5.5 Conclusion

A novel, practically more feasible and accurate deformable image registration methodology for thoracic image sequences has been proposed. It could be a boon for real-life applications such as image acquisition for radiotherapy planning of thoracic lesions, dosimetric evaluation, tumour growth progression (with time) and determination of subject-specific deformable motion models.

An effort has been made to model elastic image deformations after real life 2D elastic object deformations such that all the constituents of that object are constantly in spontaneous motion and are not at equilibrium. Motion of 2D elastic objects due to internal forces has been used as an inspiration to determine deformations in thoracic CT images. Results from our study showed average target registration error of less than 1 pixel over the entire thoracic ct image volume. Such an accurate registration of thoracic ct images obtained in the deformed state can be useful in treatment planning and also for longitudinal evaluation of progression/regression in patients with lung cancer. Although the utility of this method has been shown for ct image volume, the method can be applied to images of any other imaging modalities as well.

CHAPTER 6: CONCLUSION & FUTURE WORK

Deformable image registration is a challenging problem due to various types of possible deformations and high chance of false registration. In particular, registration of CT image stacks/sequences is a very difficult task because of the sheer number of landmark feature points involved in the registration process. DIR techniques able to account for displacement and deformation of organs in a series of medical images acquired in connection with fractions of radiotherapy are a key component in the efforts to improve the treatment guided by image data. The conclusions of work of this thesis and suggestions for future research are presented in this chapter.

6.1 Concluding Remarks

The study was set out to explore new and accurate deformable image registration techniques for thoracic CT image pairs and image sequences. The investigations were set up on a three dimensional CT image database of 10 subjects. For each subject there were 10 images in temporal sequence through all three anatomical positions i.e. axial, coronal and sagittal, out of which first six were temporally aligned with a gap of 0.1 seconds from full inhale to full exhale position. The objective was to register the image pair and sequences accurately from the above mentioned data (or any other modality image) by applying geometrical transformation based registration algorithms. Three such registration algorithms were proposed, both standalone and composite algorithms. One of the objectives of the algorithms was to determine an image registration model for a variety of breathing motion data from many subjects. It is known that different individuals have different breathing frequencies depending on many factors like their respective lifestyles, genetic or hereditary diseases etc. The study was conducted to develop algorithms to adjust and normalize these variations, thus providing a common denominator upon which more accurate analyses can be made in future, both from medical imaging and clinical research perspectives. There hasn't been a consolidated method to assess the deformations happening in the thoracic region during the process of breathing. The proposed method helps in assessing this deformation in form of average displacement of all common landmark points in that image sequence from full inhale to exhale positions. This has been implemented on all test subjects and has been demonstrated for one subject in further detail. Also, the displacing points on the image leave clear and color coordinated paths which reflect the exact motion of those points through frames of the image sequence. This would help in assessing and analysing individual motion separately at every point of the medical image if required. This would be highly beneficial in detecting abnormal behaviour in organs when compared to normal established baselines. Accuracy of these algorithms was determined using metrics like Target registration error, image similarity metrics etc. Lower values of target registration error for applied algorithms in comparison to those prevalent indicated higher deformable image registration accuracies. Likewise, similarity metrics indicating higher percentage of correspondence between the transformed image and target image (post registration) in comparison to the initial similarity between source and target image indicate better registration than the usually employed methods to achieve same objective.

6.2 Scope for Future Work

The proposed methods proved to be accurate and fulfilling the objectives keeping in mind which the work was started, they can be seen as the stepping stones to more accurate and fast techniques to achieve deformable image registration in the future. The proposed methods seem to exhaust the scope of this thesis, there are a few modifications in already existing methods and few new ideas that are in order to be taken up in the future to enhance and push the boundaries of image processing and medical imaging in particular. One of the primary modifications would be soft computing based feature point marking system. The idea is to use an automatic/semiautomatic learning based relevant landmark point marking system. Organ based information from both medical and image processing perspectives will be used as a pre-requisite for the learning procedure to enable the landmark point marker to highlight only relevant areas instead of either manually plotting points or using an automatic method which marks landmark points randomly (based on presumptions other than the medical kind). This would help in highlighting those areas of the medical image which actually do move rather than those which do not most of the time thus making better use of the resources and making the whole process faster and more relevant. The image registration resulting from these relevant common landmark point cloud would be less erroneous and more dynamic according to the organ of which the medical images are being registered.

Deformable image registration has been playing a pivotal role in correcting the ‘human error’ aspect of medical image acquisition irrespective of the image modality it is being used for and has been a major contributor in clinical research based on these images for similar reasons. The methods proposed in this work will become a small part of an already vast cluster of similar algorithms, all working in tandem towards a common objective: fast, accurate and efficient image based clinical intervention as when required.

REFERENCES

Aires, K. R., Santana, A. M., & Medeiros, A. A. (2008, March). Optical flow using color information: preliminary results. In Proceedings of the 2008 ACM symposium on Applied computing (pp. 1607-1611). ACM.

Alexa, M., Behr, J., Cohen-Or, D., Fleishman, S., Levin, D., & Silva, C. T. (2003). Computing and rendering point set surfaces. Visualization and Computer Graphics, IEEE Transactions on, 9(1), 3-15.

Al-Mayah, A., Moseley, J., & Brock, K. K. (2008). Contact surface and material nonlinearity modeling of human lungs. Physics in medicine and biology, 53(1), 305.

Ashburner, J., & Friston, K. J. (2011). Diffeomorphic registration using geodesic shooting and Gauss–Newton optimisation. NeuroImage, 55(3), 954-967.

Bajcsy, R., & Kovačič, S. (1989). Multiresolution elastic matching. Computer vision, graphics, and image processing, 46(1), 1-21.

Baker, S., Scharstein, D., Lewis, J. P., Roth, S., Black, M. J., & Szeliski, R. (2011). A database and evaluation methodology for optical flow. International Journal of Computer Vision, 92(1), 1-31.

Barron, J. L., Fleet, D. J., & Beauchemin, S. S. (1994). Performance of optical flow techniques. International journal of computer vision, 12(1), 43-77.

Bay H, Ess A, Tuytelaars T, Van Gool L (2008) SURF: Speeded Up Robust Features. Computer Vision and Image Understanding (CVIU) 110:346-359.

Bay H, Tuytelaars T, Van Gool L (2006) Surf: Speeded up robust features. Computer Vision – ECCV 2006 3951:404-417, Springer Berlin Heidelberg, Zurich.

Beauchemin, S. S., & Barron, J. L. (1995). The computation of optical flow. ACM Computing Surveys (CSUR), 27(3), 433-466.

Beuthien, B., Kamen, A., & Fischer, B. (2010). Recursive Green's function registration. In Medical Image Computing and Computer-Assisted Intervention–MICCAI 2010 (pp. 546-553). Springer Berlin Heidelberg.

Black, M. J., & Anandan, P. (1996). The robust estimation of multiple motions: Parametric and piecewise-smooth flow fields. Computer vision and image understanding, 63(1), 75-104.

Blackall JM, Ahmad S, Miquel ME, McClelland JR, Landau DB, Hawkes DJ (2006) MRI-based measurements of respiratory motion variability and assessment of imaging strategies for radiotherapy planning. Phys. Med. Biol. 51: 4147–4169.

Bookstein, F. L., & Green, W. D. (1993). A feature space for edgels in images with landmarks. Journal of Mathematical Imaging and Vision, 3(3), 231-261.

Bro-Nielsen, M., & Gramkow, C. (1996). Fast fluid registration of medical images. In Visualization in Biomedical Computing (pp. 265-276). Springer Berlin Heidelberg.

Brock, K. K., Sharpe, M. B., Dawson, L. A., Kim, S. M., & Jaffray, D. A. (2005). Accuracy of finite element model-based multi-organ deformable image registration. Medical physics, 32(6), 1647-1659.

Broit, C. (1981). Optimal registration of deformed images.

Cachier, P., Bardinet, E., Dormont, D., Pennec, X., & Ayache, N. (2003). Iconic feature based nonrigid registration: the PASHA algorithm. Computer vision and image understanding, 89(2), 272-298.

Castillo, E., Castillo, R., Fuentes, D., & Guerrero, T. (2014). SU-EJ-197: A Moving Least Squares Approach for Computing Spatially Accurate Transformations That Satisfy Strict Physiologic Constraints. Medical Physics, 41(6), 202-202.

Castillo, E., Castillo, R., Martinez, J., Shenoy, M., & Guerrero, T. (2010). Four-dimensional deformable image registration using trajectory modeling. Physics in medicine and biology, 55(1), 305.

Castillo, R., Castillo, E., Guerra, R., Johnson, V. E., McPhail, T., Garg, A. K., & Guerrero, T. (2009). A framework for evaluation of deformable image registration spatial accuracy using large landmark point sets. Physics in medicine and biology, 54(7), 1849.

Chiang, M. C., Leow, A. D., Klunder, A. D., Dutton, R. A., Barysheva, M., Rose, S. E., ... & Thompson, P. M. (2008). Fluid registration of diffusion tensor images using information theory. Medical Imaging, IEEE Transactions on, 27(4), 442-456.

Christensen, G. E., Rabbitt, R. D., & Miller, M. I. (1996). Deformable templates using large deformation kinematics. Image Processing, IEEE Transactions on, 5(10), 1435-1447.

Christensen, G. E., Joshi, S. C., & Miller, M. I. (1997). Volumetric transformation of brain anatomy. Medical Imaging, IEEE Transactions on, 16(6), 864-877.

Christensen, G. E., & Johnson, H. J. (2001). Consistent image registration. Medical Imaging, IEEE Transactions on, 20(7), 568-582.

Cornelis, N., & Gool, L. V. (2008, June). Fast scale invariant feature detection and matching on programmable graphics hardware. In Computer Vision and Pattern Recognition Workshops, 2008. CVPRW'08. IEEE Computer Society Conference on (pp. 1-8). IEEE.

Cotter, C. J., & Holm, D. D. (2006). Singular solutions, momentum maps and computational anatomy. arXiv preprint nlin/0605020.

D'Agostino, E., Maes, F., Vandermeulen, D., & Suetens, P. (2003). A viscous fluid model for multimodal non-rigid image registration using mutual information. Medical image analysis, 7(4), 565-575.

Davatzikos, C. (1997). Spatial transformation and registration of brain images using elastically deformable models. Computer Vision and Image Understanding, 66(2), 207-222.

Dupuis, P., Grenander, U., & Miller, M. I. (1998). Variational problems on flows of diffeomorphisms for image matching. Quarterly of applied mathematics, 56(3), 587.

Dykstra, A. R., Chan, A. M., Quinn, B. T., Zepeda, R., Keller, C. J., Cormier, J., Madsen, J. R., Eskandar, E. N., & Cash, S. S. (2012). Individualized localization and cortical surface-based registration of intracranial electrodes. Neuroimage, 59(4), 3563-3570.

Ehrhardt, J., Werner R, Schmidt-Richberg A, Handels H (2011) Statistical Modeling of 4D Respiratory Lung Motion Using Diffeomorphic Image Registration. Medical Imaging, IEEE Transactions on. Doi: 0.1109/TMI.2010.2076299.

Feldmar, J., & Ayache, N. (1996). Rigid, affine and locally affine registration of free-form surfaces. International journal of computer vision, 18(2), 99-119.

Fischer, B., & Modersitzki, J. (2002). Fast diffusion registration. Contemporary Mathematics, 313, 117-128.

Fischer, B., & Modersitzki, J. (2003). Curvature based image registration. Journal of Mathematical Imaging and Vision, 18(1), 81-85.

Fischer, B., & Modersitzki, J. (2004). A unified approach to fast image registration and a new curvature based registration technique. Linear Algebra and its applications, 380, 107-124.

Fleet, D., & Weiss, Y. (2006). Optical flow estimation. In Handbook of mathematical models in computer vision (pp. 237-257). Springer US.

Fuerst, B., Mansi, T., Carnis, F., Salzle, M., Zhang, J., Declerck, J., ... & Kamen, A. (2015). Patient-Specific Biomechanical Model for the Prediction of Lung Motion From 4-D CT Images. Medical Imaging, IEEE Transactions on, 34(2), 599-607.

Goitein M (2004) Organ and tumor motion: An overview. Seminars in Radiation Oncology, 14, 2–9.

Hadamard, J. (2014). Lectures on Cauchy's problem in linear partial differential equations. Courier Corporation.

Haller, J. A., Kramer, S. S., & Lietman, S. A. (1987). Use of CT scans in selection of patients for pectusexcavatum surgery: a preliminary report. Journal of pediatric surgery, 22(10), 904-906.

Heinrich, H. P., Jenkinson, M., Brady, M., & Schnabel, J. (2013). MRF-based deformable registration and ventilation estimation of lung CT. Medical Imaging, IEEE Transactions on, 32(7), 1239-1248.

Henn, S. (2006). A full curvature based algorithm for image registration. Journal of Mathematical Imaging and Vision, 24(2), 195-208.

Higham, N. J. (2005). The scaling and squaring method for the matrix exponential revisited. SIAM Journal on Matrix Analysis and Applications, 26(4), 1179-1193.

Horn, B. K., & Schunck, B. G. (1981, November). Determining optical flow. In 1981 Technical symposium east (pp. 319-331). International Society for Optics and Photonics.

Igarashi, T., Moscovich, T., and Hughes, J. F. 2005. As rigid-as-possible shape manipulation. ACM Trans. Graph. 24, 3, 1134–1141.

Jain, A. K., Zhong, Y., & Lakshmanan, S. (1996). Object matching using deformable templates. Pattern Analysis and Machine Intelligence, IEEE Transactions on, 18(3), 267-278.

Joshi, S. C., & Miller, M. I. (2000). Landmark matching via large deformation diffeomorphisms. Image Processing, IEEE Transactions on, 9(8), 1357-1370.

Kang, T. K., Choi, I. H., & Lim, M. T. (2015). MDGHM-SURF: A robust local image descriptor based on modified discrete Gaussian–Hermite moment. Pattern Recognition, 48(3), 670-684.

Keall PJ et al. (2006) The management of respiratory motion in radiation oncology report of AAPM task group 76. Medical Physics 33:3874–3900.

Kim, H. C., Park, H. J., Nam, K. W., Kim, S. M., Choi, E. J., Jin, S., ... & Kim, M. G. (2010). Fully automatic initialization method for quantitative assessment of chest-wall deformity in funnel chest patients. Medical & biological engineering & computing, 48(6), 589-595.

Koenderink, J. J. (1984). The structure of images. Biological cybernetics, 50(5), 363-370.

Kybic, J., & Unser, M. (2003). Fast parametric elastic image registration. Image Processing, IEEE Transactions on, 12(11), 1427-1442.

Lancaster, P., & Salkauskas, K. (1981). Surfaces generated by moving least squares methods. Mathematics of computation, 37(155), 141-158.

Leow, A., Huang, S. C., Geng, A., Becker, J., Davis, S., Toga, A., & Thompson, P. (2005, July). Inverse consistent mapping in 3D deformable image registration: its construction and statistical properties. In Information Processing in Medical Imaging (pp. 493-503). Springer Berlin Heidelberg.

Lindeberg, T. (1998). Feature detection with automatic scale selection. International journal of computer vision, 30(2), 79-116.

Lucas, B. D., & Kanade, T. (1981, August). An iterative image registration technique with an application to stereo vision. In IJCAI (Vol. 81, pp. 674-679).

Malis, E. (2004, April). Improving vision-based control using efficient second-order minimization techniques. In Robotics and Automation, 2004. Proceedings. ICRA'04. 2004 IEEE International Conference on (Vol. 2, pp. 1843-1848). IEEE.

Markelj, P., Tomaževič, D., Likar, B., & Pernuš, F. (2012). A review of 3D/2D registration methods for image-guided interventions. Medical image analysis, 16(3), 642-661.

Marsland, S., & McLachlan, R. (2007, July). A Hamiltonian particle method for diffeomorphic image registration. In Information Processing in Medical Imaging (pp. 396-407). Springer Berlin Heidelberg.

Marsland, S., & Twining, C. J. (2004). Constructing diffeomorphic representations for the groupwise analysis of nonrigid registrations of medical images. Medical Imaging, IEEE Transactions on, 23(8), 1006-1020.

Mcgregor, B. (1998). Automatic registration of images of pigmented skin lesions. Pattern Recognition, 31(6), 805-817.

Mikolajczyk, K.; Schmid, C., "Indexing based on scale invariant interest points," in Computer Vision, 2001. ICCV 2001. Proceedings. Eighth IEEE International Conference on , vol.1, no., pp.525-531 vol.1, 2001

Modersitzki, J. (2004). Numerical methods for image registration. Oxford university press.

Moler, C., & Van Loan, C. (2003). Nineteen dubious ways to compute the exponential of a matrix, twenty-five years later. SIAM review, 45(1), 3-49.

Muenzing SEA, Van Ginnekan B, Viergever MA, Pluim JPW (2014) DIRBoost-an algorithm for boosting deformable image registration: application to lung CT intra-subject registration. Medical Image Analysis, Elsevier 18, 449-459.

Murphy, K., Van Ginneken, B., Reinhardt, J. M., Kabus, S., Ding, K., Deng, X., ... & Vercauteren, T. (2011). Evaluation of registration methods on thoracic CT: the EMPIRE10 challenge. Medical Imaging, IEEE Transactions on, 30(11), 1901-1920.

Nakagomi, K., Shimizu, A., Kobatake, H., Yakami, M., Fujimoto, K., & Togashi, K. (2013). Multi-shape graph cuts with neighbor prior constraints and its application to lung segmentation from a chest CT volume. Medical image analysis, 17(1), 62-77.

Nehmeh SA, Erdi YE, Pan T et al (2004) Quantitation of respiratory motion during 4D-PET/CT acquisition. Med. Phys., vol. 31, no. 6, pp. 1333–1338, 2004.

Oliviera FPM, Tavares JMRS (2012) Medical Image Registration: a Review. Computer methods in Biomechanics and Biomedical Engineering 17, 73-93.

Pang et al. (2012) Fully affine invariant SURF for image matching. Neurocomputing 85:6-10, ISSN 0925-2312.

Pedersen, J. T., (Q4 2011) SURF: Feature detection & description, jtp@cs.au.dk.

Pennec, X., Stefanescu, R., Arsigny, V., Fillard, P., & Ayache, N. (2005). Riemannian elasticity: A statistical regularization framework for non-linear registration. In Medical Image Computing and Computer-Assisted Intervention–MICCAI 2005 (pp. 943-950). Springer Berlin Heidelberg.

Peyrat, J. M., Delingette, H., Sermesant, M., Pennec, X., Xu, C., & Ayache, N. (2008). Registration of 4D time-series of cardiac images with multichannel diffeomorphic demons. In Medical Image Computing and Computer-Assisted Intervention–MICCAI 2008 (pp. 972-979). Springer Berlin Heidelberg.

Rabbitt, R. D., Weiss, J. A., Christensen, G. E., & Miller, M. I. (1995, August). Mapping of hyperelastic deformable templates using the finite element method. In SPIE's 1995 International Symposium on Optical Science, Engineering, and Instrumentation (pp. 252-265). International Society for Optics and Photonics.

Reinhardt JM, Ding K, Cao K, Christensen GE, Hoffman EA, Bodas SV (2008) Registration-based estimates of local lung tissue expansion compared to Xenon CT measures of specific ventilation. Med. Image Anal., vol. 12, no. 6, pp. 752–763.

Rohr, K., Stiehl, H. S., Sprengel, R., Buzug, T. M., Weese, J., & Kuhn, M. H. (2001). Landmark-based elastic registration using approximating thin-plate splines. Medical Imaging, IEEE Transactions on, 20(6), 526-534.

Sarrut D, Boldea V, Miguet S, Ginestet C (2006) Simulation of four-dimensional CT images from deformable registration between inhale and exhale breath-hold CT scans. Med. Phys., vol. 33, no. 3, pp. 605–617.

Sato, A. K., Stevo, N. A., Tavares, R. S., Tsuzuki, M. S. G., Kadota, E., Gotoh, T., Kagei, S. & Iwasawa, T. (2011). Registration of temporal sequences of coronal and sagittal MR images through respiratory patterns. Biomedical Signal Processing and Control, 6(1), 34-47.

Schaefer, S., McPhail, T., & Warren, J. (2006, July). Image deformation using moving least squares. In ACM Transactions on Graphics (TOG) (Vol. 25, No. 3, pp. 533-540). ACM.

Silva, E. A., Panetta, K., & Agaian, S. S. (2007, April). Quantifying image similarity using measure of enhancement by entropy. In Defense and Security Symposium (pp. 65790U-65790U). International Society for Optics and Photonics.

So, R. W., Tang, T. W., & Chung, A. C. (2011). Non-rigid image registration of brain magnetic resonance images using graph-cuts. Pattern Recognition, 44(10), 2450-2467.

Sotiras, A., Davatzikos, C., & Paragios, N., (2013) Deformable Medical Image Registration: A Survey. IEEE Transactions on Medical Imaging 32, 1153-1190.

Stefanescu, R., Pennec, X., & Ayache, N. (2004). Grid powered nonlinear image registration with locally adaptive regularization. Medical image analysis, 8(3), 325-342.

Stevo, N., Campos, R., Tavares, R. S., Tsuzuki, M. D. S. G., Gotoh, T., Kagei, S., Iwasawa, T., (2009) Registration of temporal sequences of coronal and sagittal images obtained from magnetic resonance. Proceedings of XX International Congress of Mechanical Engineering.

Sull, S., & Ahuja, N. (1995). Integrated matching and segmentation of multiple features in two views. Computer vision and image understanding, 62(3), 279-297.

Sun, D., Roth, S., & Black, M. J. (2014). A quantitative analysis of current practices in optical flow estimation and the principles behind them. International Journal of Computer Vision, 106(2), 115-137.

Sundaram, T. A., & Gee, J. C. (2005). Towards a model of lung biomechanics: pulmonary kinematics via registration of serial lung images. Medical image analysis, 9(6), 524-537.

Szeliski, R., & Coughlan, J. (1994, June). Hierarchical spline-based image registration. In Computer Vision and Pattern Recognition, 1994. Proceedings CVPR'94., 1994 IEEE Computer Society Conference on (pp. 194-201). IEEE.

Szeliski, R., & Coughlan, J. (1997). Spline-based image registration. International Journal of Computer Vision, 22(3), 199-218.

Thirion, J. P. (1998). Image matching as a diffusion process: an analogy with Maxwell's demons. Medical image analysis, 2(3), 243-260.

Thomson, W. (1874). 9. The Kinetic Theory of the Dissipation of Energy. Proceedings of the Royal Society of Edinburgh, 8, 325-334.

Trouvé, A. (1998). Diffeomorphisms groups and pattern matching in image analysis. International Journal of Computer Vision, 28(3), 213-221.

Tsui, B. M., Segars WP, Lalush DS (2000) Effects of Upward Creep and Respiratory Motion in Myocardial SPECT. IEEE Transactions on Nuclear Science, v. 47, pp. 1192-1195.

Ugural, A. C., & Fenster, S. K. (2003). Advanced strength and applied elasticity. Pearson education.

Vedam SS, Keall PJ, Docef A, Todor DA, Kini VR, Mohan R (2004) Predicting respiratory motion for four-dimensional radio-therapy. Med. Phys., vol. 31, no. 8, pp. 2274–2283.

Vercauteren, T., Pennec, X., Malis, E., Perchant, A., & Ayache, N. (2007, July). Insight into efficient image registration techniques and the demons algorithm. In Information Processing in Medical Imaging (pp. 495-506). Springer Berlin Heidelberg.

Viola, P., & Jones, M. (2001). Rapid object detection using a boosted cascade of simple features. In Computer Vision and Pattern Recognition, 2001. CVPR 2001. Proceedings of the 2001 IEEE Computer Society Conference on (Vol. 1, pp. I-511). IEEE.

Wang, Y., & Staib, L. H. (2000). Physical model-based non-rigid registration incorporating statistical shape information. Medical image analysis, 4(1), 7-20.

Wang, Z., Bovik, A. C., Sheikh, H. R., & Simoncelli, E. P. (2004). Image quality assessment: from error visibility to structural similarity. Image Processing, IEEE Transactions on, 13(4), 600-612.

Warren, D. H., & Strelow, E. R. (1985). Sensory substitution in blind children and neonates. In Electronic Spatial Sensing for the Blind (pp. 273-298). Springer Netherlands.

Xiong, G., Chen, C., Chen, J., Xie, Y., & Xing, L. (2012). Tracking the motion trajectories of junction structures in 4D CT images of the lung. Physics in medicine and biology, 57(15), 4905.

Yanovsky, I., Le Guyader, C., Leow, A., Toga, A., Thompson, P., & Vese, L. (2008, October). Unbiased volumetric registration via nonlinear elastic regularization. In 2nd MICCAI Workshop on Mathematical Foundations of Computational Anatomy.

Yeo, B. T., Vercauteren, T., Fillard, P., Peyrat, J. M., Pennec, X., Golland, P., ... & Clatz, O. (2009). DT-REFinD: Diffusion tensor registration with exact finite-strain differential. Medical Imaging, IEEE Transactions on, 28(12), 1914-1928.

Yeo, B. T., Sabuncu, M. R., Vercauteren, T., Ayache, N., Fischl, B., & Golland, P. (2010). Spherical demons: fast diffeomorphic landmark-free surface registration. Medical Imaging, IEEE Transactions on, 29(3), 650-668.

Yoon H, Chung H, Hahn H (2009) SURF algorithm with color and global characteristics. ICCAS-SICE 2009. 183-187.

Zhang, B., Arola, D. D., Roys, S., & Gullapalli, R. P. (2011). Three-dimensional elastic image registration based on strain energy minimization: application to prostate magnetic resonance imaging. Journal of digital imaging, 24(4), 573-585.

Zhang, T., Orton, N. P., Mackie, T. R., & Paliwal, B. R. (2004). Technical note: A novel boundary condition using contact elements for finite element based deformable image registration. Medical physics, 31(9), 2412-2415.

Zhang, Y., Yang, J., Zhang, L., Balter, P. A., & Dong, L. (2013). Modeling respiratory motion for reducing motion artifacts in 4D CT images. Medical physics, 40(4), 041716.

Zitova, B., & Flusser, J. (2003). Image registration methods: a survey. Image and vision computing, 21(11), 977-1000.

Zordan VB, Celly B, Chiu B, DiLorenzo PC (2004) Breathe Easy: Model and Control of Simulated Respiration for Animation. Proceedings of the 2004 ACM SIGGRAPH/Eurographics symposium on Computer animation, Grenoble, France.

http://www.dir-lab.com/Motivation.html.

APPENDIX

Appendix-A: Geometrical Deformation models for elastic images

Table A.1: Elastic Body Models

Author	Year	Title	About	Method	Findings	Remarks
M. Droske et al.	2004	A variational approach to non rigid morphological image registration	A novel variational method to non rigid registration of multi-modal data.	A suitable deformation was determined via the minimization of a morphological i.e., contrast invariant, matching functional along with an appropriate regularization energy.	It was found suitable for the registration of multimodal data, as confirmed by some numerical results.	
A. leow et al.	2005	Inverse consistent mapping in 3D deformable image registration: Its construction and statistical properties	A new approach to inverse consistent image registration. A uni-directional algorithm is developed using symmetric cost functionals and regularizers.	Instead of enforcing inverse consistency using an additional penalty that penalizes inconsistency error, the new algorithm directly models the backward mapping by inverting the forward mapping. The resulting minimization problem could then be solved uni-directionally involving only the forward mapping, without optimizing in the backward direction.	The algorithm was evaluated by applying it to the serial MRI scans of a clinical case of semantic dementia. The statistical distributions of the local volume change (Jacobian) maps were examined by considering the Kullback-Liebler distances on the material density functions.	Statistically significant differences were detected between consistent versus inconsistent matching when permutation tests were performed on the resulting deformation maps.

X. Pennec et al.	2005	Riemannian elasticity: A statistical regularization framework for non-linear registration	The elastic energy has been interpreted as the distance of the Green-St Venant strain tensor to the identity, which reflects the deviation of the local deformation from a rigid transformation.	By changing the Euclidean metric for a more suitable Riemannian one, a consistent statistical framework is defined to quantify the amount of deformation. These statistics are then used as parameters in a Mahalanobis distance to measure the statistical deviation from the observed variability, giving a new regularization criterion that we called the statistical Riemannian elasticity.	It was found that the new criterion is able to handle anisotropic deformations and is inverse-consistent.	Preliminary results showed that it can be quite easily implemented in a non-rigid registration algorithm.
A.D. Leow et al.	2007	Statistical properties of Jacobian maps and the realization of unbiased large-deformation nonlinear image registration	A method has been proposed to provide rigorous mathematical analyses of the Jacobian maps, and use them to motivate a new numerical method to construct unbiased nonlinear image registration.	It is established that that logarithmic transformation is crucial for analyzing Jacobian values representing morphometric differences. Statistical distributions of log-Jacobian maps are examined by defining the Kullback-Leibler (KL) distance on material density functions arising in continuum-mechanical models.	symmetrization of image registration statistically reduces skewness in the log-Jacobian map.	
I. Yanovsky et al.	2008	Unbiased volumetric registration via nonlinear elastic	A new nonlinear image registration model	The nonlinear elastic and the unbiased regularization terms are	The new unbiased nonlinear elasticity model was	

		regularization	which is based on nonlinear elastic regularization and unbiased registration.	simplified using the change of variables by introducing an unknown that approximates the Jacobian matrix of the displacement field. This reduces the minimization to involve linear differential equations. The new model is written in a unified variational form and is minimized using gradient descent.	found to be computationally more efficient and easier to implement than the unbiased fluid registration. The unbiased large-deformation nonlinear elasticity method was tested using volumetric serial magnetic resonance images and showed advantages for medical imaging applications.	
C.L. Guyader & L.A. Vese	2011	A combined segmentation and registration framework with a nonlinear elasticity smoother	A new non-parametric combined segmentation and registration method.	The modeling is twofold: first, registration is jointly performed with segmentation since guided by the segmentation process; it means that the algorithm produces both a smooth mapping between the two shapes and the segmentation of the object contained in the reference image. Secondly, the use of a nonlinear-elasticity-type regularizer allows large deformations to occur, which makes the model comparable in this point with the viscous fluid registration method.	The shapes to be matched were viewed as Ciarlet–Geymonat materials. Existence of minimizers of the introduced functional was proved and an approximated problem based on the Saint Venant–Kirchhoff stored energy for the numerical implementation and solved by an augmented Lagrangian technique.	Several applications are proposed here to demonstrate the potential of this method to both segmentation of one single image and to registration between two images.

Table A.2: Viscous Fluid Flow Model

Author	Year	Title	About	Method	Findings	Remarks
W.R. Crum et al.	2005	Anisotropic multi-scale fluid registration: Evaluation in magnetic resonance breast imaging	A multi-resolution fluid registration algorithm which improves on previous works on multiple levels of free form deformation (FFD).	Directly solving the Navier-Stokes equation at the resolution of the images; accommodating image sampling anisotropy using semi-coarsening and implicit smoothing in a full multi-grid (FMG) solver; and exploiting the inherent multi-resolution nature of FMG to implement a multi-scale approach.	Evaluation was on five magnetic resonance (MR) breast images subject to six biomechanical deformation fields over 11 multi-resolution schemes. Quantitative assessment was by tissue overlaps and target registration errors and by registering using the known correspondences rather than image features to validate the fluid model.	The results showed that fluid registration of 3D breast MR images to sub-voxel accuracy is possible in minutes on a 1.6 GHz Linux-based Athlon processor with coarse solutions obtainable in a few tens of seconds. Accuracy and computation time are comparable to FFD techniques validated for this application.
N.D. Cahill et al.	2007	Fourier methods for nonparametric image registration	It was shown that Fourier methods can be employed to quickly solve the linear PDE systems for every combination of standard regularizers (diffusion, curvature, elastic, and fluid) and boundary conditions (Dirichlet, Neumann, and periodic).	Faster techniques based on Fourier methods, multigrid methods, and additive operator splitting; exist for solving the linear PDE systems for specific combinations of regularizers and boundary conditions were applied on a	Fourier methods can be employed to quickly solve the linear PDE systems for every combination of standard regularizers.	

				mammography image set.		
M.-C. Chiang et al.	2008	Fluid registration of diffusion tensor images using information theory	This work presented an information-theoretic cost metric, symmetrised Kullback-Leibler (sKL) divergence, or *J*-divergence, to fluid registration of diffusion tensor images.	Three-dimensional DTI data from 34 subjects were fluidly registered to an optimized target image. The flow was regularized with a large-deformation diffeomorphic mapping based on the kinematics of a Navier-Stokes fluid. A driving force was developed to minimize the J-divergence between the deforming source and target diffusion functions, while reorienting the flowing tensors to preserve fiber topography.	It was showed that the sKL-divergence based on full diffusion PDFs is adaptable to higher-order diffusion models, such as high angular resolution diffusion imaging (HARDI). The sKL-divergence was sensitive to subtle differences between two diffusivity profiles, showing promise for nonlinear registration applications and multi subject statistical analysis of HARDI data.	

Table A.3: Diffusion Model

Author	Year	Title	About	Method	Findings	Remarks
J.M. Peyrat et al.	2008	Registration of 4D time-series of cardiac images with multichannel diffeomorphic demons	A generic framework for intersubject non-linear registration of 4D time-series images.	Spatio-temporal registration is defined by mapping trajectories of physical points as opposed to spatial registration that solely aims at mapping homologous points. The trajectories were determined which had to be registered in each sequence using a motion tracking algorithm based on the Diffeomorphic Demons algorithm. Simultaneously pairwise registrations were performed of corresponding time-points with the constraint to map the same physical points over time.	It was shown that this trajectory registration can be formulated as a multichannel registration of 3D images.	This framework is applied to the inter-subject non-linear registration of 4D cardiac CT sequences.

BTT Yeo et al.	2009	DT-REFinD: Diffusion tensor registration with exact finite-strain differential	The DT-REFinD algorithm for the diffeomorphic nonlinear registration of diffusion tensor images.	Results were borrowed from the pose estimation literature in computer vision to derive an analytical gradient of the registration objective function. By utilizing the closed-form gradient and the velocity field representation of one parameter subgroups of diffeomorphisms, the resulting registration algorithm came to be diffeomorphic and fast. The algorithm was contrasted and compared with a traditional FS alternative that ignores the reorientation in the gradient computation.	It was shown that the exact gradient leads to significantly better registration at the cost of computation time. Alignment quality was assessed with a battery of metrics including tensor overlap, fractional anisotropy, inverse consistency and closeness to synthetic warps.	The improvements persist even when a different reorientation scheme, preservation of principal directions, was used to apply the final deformations.
M. Modat et al.	2010	Diffeomorphic demons using normalized mutual information, evaluation on multimodal brain MR images	A diffeomorphic demons implementation using the analytical gradient of Normalised Mutual Information (NMI) in a conjugate gradient optimiser.	Hailed as the first reported qualitative and quantitative assessment of the demons for inter-modal registration.	Experiments to spatially normalise real MR images, and to recover simulated deformation fields, demonstrated similar accuracy from NMI-demons and classical demons when the latter may be used, and similar	

					accuracy for NMI-demons on T1w–T1w and T1w–T2w registration.	
BTT Yeo et al.	2010	Spherical demons: Fast diffeomorphic landmark-free surface registration	The Spherical Demons algorithm for registering two spherical images.	Exploiting spherical vector spline interpolation theory, it was shown that a large class of regularizors for the modified Demons objective function can be efficiently approximated on the sphere using iterative smoothing. Based on one parameter subgroups of diffeomorphisms, the resulting registration is diffeomorphic and fast. The Spherical Demons algorithm can also be modified to register a given spherical image to a probabilistic atlas.	Two variants of the algorithm corresponding to warping the atlas or warping the subject were demonstrated. Registration of a cortical surface mesh to an atlas mesh, both with more than 160 k nodes requires less than 5 min when warping the atlas and less than 3 min when warping the subject on a Xeon 3.2 GHz single processor machine. This is comparable to the fastest non diffeomorphic landmark-free surface registration algorithms.	Technique was validated in two different applications that use registration to transfer segmentation labels onto a new image 1) parcellation of in vivo cortical surfaces and 2) Brodmann area localization in ex vivo cortical surfaces.

Table A.4: Curvature Registration

Author	Year	Title	About	Method	Findings	Remarks
B. Glocker et al.	2009	Approximated curvature penalty in non-rigid registration using pairwise MRFs	An approximated curvature penalty using second-order derivatives defined on the MRF pairwise potentials is proposed.	Labeling of discrete Markov Random Fields (MRFs) for solving the problem of non-rigid image registration. Smoothness is achieved by penalizing the derivatives of the displacement field.	It was demonstrated that the approximated term has similar properties as higher-order approaches (invariance to linear transformations), while the computational efficiency of pair wise models remained preserved.	
B. Beuthien et al.	2010	Recursive Green's function registration	It has been tried to minimize a joint functional that is comprised of a similarity measure and a regularizer in order to obtain a reasonable displacement field that transforms one image to the other.	A generalized and efficient numerical scheme for solving such system of PDEs simply by applying 1-dimensional recursive filtering to the right hand side of the system based on the Green's function of the differential operator that corresponds to the chosen regularizer.	The associated Green's function for the diffusive and curvature regularizers was presented and it was shown that how one may efficiently implement the whole process by using recursive filter approximation.	

Table A.5: Flows of Diffeomorphisms

Author	Year	Title	About	Method	Findings	Remarks
M. Hernandez et al.	2009	Registration of anatomical images using paths of diffeomorphisms parameterized with stationary vector field flows	Proposed paradigm for diffeomorphic registration is the Large Deformation Diffeomorphic Metric Mapping (LDDMM). In this framework, transformations are characterized as end points of paths parameterized by time-varying flows of vector fields defined on the tangent space of a Riemannian manifold of diffeomorphisms and computed from the solution of the non-stationary transport equation associated to these flows.	Optimization in LDDMM is performed on the space of non-stationary vector field flows resulting into a time and memory consuming algorithm. The stationary parameterization is included for diffeomorphic registration in the LDDMM framework. The variational problem related to this registration scenario is formulated and associated Euler-Lagrange equations are derived.	The performance of the non-stationary vs. the stationary parameterizations in real and simulated 3D-MRI brain datasets is evaluated. Compared to the non-stationary parameterization, proposed method provides similar results in terms of image matching and local differences between the diffeomorphic transformations while drastically reducing memory and time requirements.	

M.D. Craene et al.	2009	Large diffeomorphic FFD registration for motion and strain quantification from 3D-US sequences	A new registration method for the in vivo quantification of cardiac deformation from a sequence of possibly noisy images.	In the proposed method, referred to as Large Diffeomorphic Free Form Deformation (LDFFD), the displacement field at each time step is computed from a smooth non-stationary velocity field, thus imposing a coupling between the transformations at successive time steps. Main contribution is to extend this framework to the estimation of motion and deformation in an image sequence. Similarity is captured for the entire image sequence using an extension of the pairwise mutual information metric. The LDFFD algorithm is applied here to recover longitudinal strain curves from healthy and Left-Bundle	Strain curves for the healthy subjects were in accordance with the literature. For the LBBB patient, strain quantified before and after Cardiac Resynchronization Therapy showed a clear improvement of cardiac function in this subject, in accordance with clinical observations.	

				Branch Block (LBBB) subjects.		
J. Ashburner et al.	2011	Diffeomorphic registration using geodesic shooting and Gauss-Newton optimisation	A nonlinear image registration algorithm based on the setting of Large Deformation Diffeomorphic Metric Mapping (LDDMM), but with a more efficient optimisation scheme, both in terms of memory required and the number of iterations required in reaching convergence.	Instead of performing a variational optimisation on a series of velocity fields, the algorithm is formulated to use a geodesic shooting procedure, so that only an initial velocity is estimated. A Gauss-Newton optimisation strategy is used to achieve faster convergence.	The algorithm was evaluated using freely available manually labelled datasets, and found to compare favourably with other inter-subject registration algorithms evaluated using the same data.	-
L. Risser et al.	2011	Simultaneous multi-scale registration using large deformation diffeomorphic metric mapping	A practical methodology to integrate prior knowledge about the registered shapes in the regularizing metric.	First presented the notion of characteristic scale at which image features are deformed. Then proposes a methodology to compare anatomical shape variations in a multi-scale	Ability of the proposed method is compared to segregate a group of subjects having Alzheimer's disease and a group of controls with a classical coarse to fine approach, on standard 3D MR	The method registers accurately volumetric images containing feature differences at several scales simultaneously with smooth deformations.

				fashion, i.e., at several characteristic scales simultaneously. In this context, a strategy was proposed to quantitatively measure the feature differences observed at each characteristic scale separately.	longitudinal brain images. It was finally applied to quantify the anatomical development of the human brain from 3D MR longitudinal images of pre-term babies.	
G. Auzias et al.	2011	Diffeomorphic brain registration under exhaustive sulcal constraints	A global, geometric approach that performs the alignment of the exhaustive sulcal imprints (cortical folding patterns) across individuals.	The DIffeomorphic Sulcal-based COrtical (DISCO) technique proceeded to the automatic extraction, identification and simplification of sulcal features from T1-weighted Magnetic Resonance Image (MRI) series. These features are then used as control measures for fully-3-D diffeomorphic deformations.	Quantitative and qualitative evaluations showed that DISCO correctly aligns the sulcal folds and gray and white matter volumes across individuals. The comparison with a recent, iconic diffeomorphic approach (DARTEL) highlighted how the absence of explicit cortical landmarks may lead to the misalignment of cortical sulci.	DISCO can also be combined with (DARTEL) to further improve the consistency and accuracy of alignment performances.

Appendix-B: Table B.1: Tabular Literature Survey, Chapter 3

Author	Year	Title	About	Method	Findings	Remarks
M. Alexa et al.	2003	Computing and rendering point set surfaces	Use of point sets to represent shapes. Defining surfaces from a set of points close to an original surface, this is approximated using MLS.	A projection procedure is defined which projects any point near the point set onto the surface. Then, the MLS surface is defined as the points projecting onto themselves. The smoothness conjecture is motivated and respective projection is computed	The proposed model was tested on 'the Stanford bunny' along with other models. The proposed approach showed smoother silhouettes and more accurate highlights in comparison to more traditional methods like **Splatting** and **Gouraud-shaded mesh** model.	Thus, it is possible to provide a point set representation that conforms to a specified tolerance. The use of a point set (without connectivity) as a representation of shapes.
S. Schaefer et al.	2006	Image deformation using moving least squares	An image deformation method based on Moving Least Squares using various classes of linear functions including affine, similarity and rigid transformations. These deformations are realistic and give the user the impression of manipulating real-world objects.	Image deformations were built based on collections of points with which the user controls the deformation. A deformation function was constructed satisfying the three properties of Interpolation, Smoothness & Identity using MLS.	The proposed method was applied for Affine, Similarity, Rigid & Elastic deformations on a set of images. It was found to perform deformations faster than the contemporary methods.	It was showed how solutions could be computed directly from the closed-form deformation using similarity transformations thereby bypassing the non-linear minimization. The method is general enough to accommodate different distance metrics dependent on the

						topology of the shape rather than the simple, Euclidean distance used as our weight factor.
P. Lancaster , K. Salkauskas	1981	Surfaces generated by moving least squares methods	An analysis of least squares methods for smoothing and interpolating scattered data was presented. In particular, theorems are proved concerning the smoothness of interpolants and the description of MLS processes as projection methods.	A non-interpolating least squares method as an alternate representation of the local approximation based on the choice of weight functions.	The differences between interpolating and non-interpolating MLS method as projection methods. The effects of the choice of weight functions and the asymptotic behaviour of such single variable and multivariate functions.	NA
R. Castillo et al.	2009	A framework for evaluation of deformable image registration spatial accuracy using large landmark point sets	Deformable Image Registration using Moving least squares for corresponding sets of feature landmark point pairs.	APRIL (Matlab based in house sw UI) for manual selection of landmark feature points. This point set is subjected to MLS, which registers the source landmark point set to the corresponding target point set.	U_{SE} α $1/(L_{PP})^{1/2}$ U_{SE} α SD_{SE} The uncertainty of spatial error estimates was found to be inversely proportional to the square root of the number of landmark point pairs and directly proportional to the standard deviation of spatial errors.	No proposition on the estimation of deformity between the registered image pairs.
K. Murphy et al.	2011	Evaluation of Registratio	EMPIRE10 (Evaluation of Methods	Methods on comparison: Asclepios1,	All methods were fully automatic with	The EMPIRE10 challenge

		n Methods on Thoracic CT: The EMPIRE10 Challenge	for Pulmonary Image REgistration 2010) is a public platform for fair and meaningful comparison of registration algorithms which are applied to a database of intrapatient thoracic CT image pairs. Evaluation of non-rigid registration techniques.	Asclepios2, CMS, DIKU, DROP, elastix, IMI Lubeck Diffeomorph, Lyon FFD, MGH, Nifty Reggers, OFDP, picsl exp, picsl gsyn, Robust TreeReg Leuven, Spline MIRIT Leuven.	the exception of MGH. Generic registration algorithms can perform better than data specific methods. It may still be the case that combining aspects of both could improve performance even further, particularly on more difficult scan pairs.	enabled detailed, independent and fair evaluation of non-rigid registration algorithms.
E. Castillo et al.	2014	A Moving Least Squares Approach for Computing Spatially Accurate Transformations That Satisfy Strict Physiologic Constraints	Computation of a physiologically realistic spatial transformation from a sparse point cloud of displacement estimates using MLS and any combination of upper bound, lower bound, or equality constraints placed on the Jacobian.	MLS defined a spatial transformation from a sparse point cloud of estimated displacements and provided simple analytic derivative estimates for all voxel locations. Given displacement estimates from automated block	Two MLS transformations were computed for five (5) pairs of inhale-exhale thoracic CT images, one with no Jacobian constraints and the other with strict contraction Jacobian constraints. Despite registering from inhale-exhale, the constrained MLS yielded a strict contraction (all Jacobian values between 0 and 1) while the unconstrained MLS resulted in regions of expansion.	The proposed MLS approach was found capable of producing Jacobian constrained transformations without degrading spatial accuracy.

Appendix-C: Table C.1: Tabular Literature Survey, Chapter 4

Author	Year	Title	About	Method	Findings	Remarks
D. Sarrut et al.	2006	Simulation of four-dimensional CT images from deformable registration between inhale and exhale breath-hold CT scans	Simulation of an artificial four-dimensional (4-D) CT image of the thorax during breathing. It is performed by deformable registration of two CT scans acquired at inhale and exhale breath-hold.	Dense deformable registrations were performed. The method was a minimization of the sum of squared differences (SSD) using an approximated second-order gradient.	Statistically better results than the reference method. The mean (and standard deviation) of distances between automatically found landmark positions and landmarks set by experts were 2.7(1.1) mm with APLDM, and 6.3(3.8) mm. The mean difference between automatic and manual landmark positions for intermediate CT images was 2.6(2.0)mm.	The generation of 4-D CT images by deformable registration of inhale and exhale CT images is feasible. This can lower the dose needed for 4-D CT acquisitions or can help to correct 4-D acquisition artifacts. The 4-D CT model can be used to propagate contours, to compute a 4-D dose map, or to simulate CT acquisitions with an irregular breathing signal. It could serve as a basis for 4-D radiation therapy planning.
N. Stevo et al.	2009	Registration of Temporal Sequences of Coronal and Sagittal Images Obtained from Magnetic Resonance	For each image in coronal and sagittal MRI sequences, the information contained in the intersection segment was determined, and the matching is done to determine the best sagittal	One of the registration approaches used is determining the distance between the images by comparing pixel by pixel and combining these differences in a single value. The other one is Fourier	The resulting pairs from both algorithms were different. It was noticed that both pairs have a satisfactory visual registration. The temporal sequence of images represented discrete instants in time, and such an almost	The temporal registration algorithm based on pixel by pixel comparison and Fourier transform showed several satisfactory results, however it is not possible to overcome the temporal low rate of image acquisition.

			images for each coronal image and vice-versa. The registration is the determination of the best images in a sequence that fits a chosen image in another sequence.	Transform based.	perfect fitting is very rare.	One of the future works would be the definition of a new registration algorithm combining pixel comparison and time segmentation.
E. Castillo et al.	2010	Four-dimensional deformable image registration using trajectory modeling	A four-dimensional deformable image registration (4D DIR) algorithm, referred to as 4D local trajectory modelling (4DLTM), is presented and applied to thoracic 4D computed tomography (4DCT) image sets.	The method exploits the incremental continuity present in 4DCT component images to calculate a dense set of parameterized voxel trajectories through space as functions of time. The spatial accuracy of the 4DLTM algorithm is compared with an alternative registration approach in which component phase to phase (CPP) DIR is utilized to determine the full displacement between maximum inhale and exhale	Cubic polynomials were found to provide sufficient flexibility and spatial accuracy for describing the point trajectories through the expiratory phases. The resulting average spatial error between the maximum phases was 1.25 mm for the 4DLTM and 1.44 mm for the CPP.	The 4DLTM method captures the long-range motion between 4DCT extremes with high spatial accuracy.

				images.		
J. Ehrhardt et al.	2011	Statistical Modeling of 4D Respiratory Lung Motion Using Diffeomorphic Image Registration	An approach to generate a mean motion model of the lung based on thoracic 4D computed tomography (CT) data of different patients to extend the motion modeling capabilities.	The modeling process consisted of three steps: an intra-subject registration to generate subject-specific motion models, the generation of an average shape and intensity atlas of the lung as anatomical reference frame, and the registration of the subject-specific motion models to the atlas in order to build a statistical 4D mean motion model (4D-MMM). In all steps, a symmetric diffeomorphic nonlinear intensity-based registration method was employed.	The model was evaluated by applying it for estimating respiratory motion of ten lung cancer patients. The prediction was evaluated with respect to landmark and tumor motion, and the quantitative analysis resulted in a mean target registration error (TRE) of 3.3 ±1.6 mm. With regard to lung tumor motion, it was shown that prediction accuracy is independent of tumor size and motion amplitude in the considered data set.	The statistical respiratory motion model is capable of providing valuable prior knowledge in many fields of applications. We present two examples of possible applications in radiation therapy and image guided diagnosis.
A.K. Sato et al.	2011	Registration of temporal sequences of coronal and sagittal MR images through respiratory patterns	This work discussed the determination of the breathing patterns in time sequence of images obtained from	A time sequence of this intersection segment of orthogonal coronal and sagittal sequences were stacked, defining a two-dimensi	The results of the proposed method in the form of synchronised sequences are compared with the pixel-by-pixel comparison method.	The proposed method increases the number of registered pairs representing composed images and allows an easy check of the breathing

			magnetic resonance (MR) and their use in the temporal registration of coronal and sagittal images.	on spatio-temporal (2DST) image. An interval Hough transform algorithm searches for synchronized movements with the respiratory function. A greedy active contour algorithm adjusts small discrepancies originated by asynchronous movements in the respiratory patterns.		phase.
G. Xiong et al.	2012	Tracking the motion trajectories of junction structures in 4D CT images of the lung	A novel method to detect a large collection of natural junction structures in the lung and use them as the reliable markers to track the lung motion.	The image intensities within a small region of interest surrounding the center are selected as its signature. Under the assumption of the cyclic motion, the trajectory was described by a closed B-spline curve and search for the control points by maximizing a metric of combined correlation coefficients. Local extrema are suppressed	The method was applied to 13 real 4D CT images. More than 700 junctions in each case are detected with an average positive predictive value of greater than 90%. The average tracking error between automated and manual tracking is sub-voxel and smaller than the published results using the same set of data.	--

				by improving the initial conditions using random walks from pair-wise optimizations . Several descriptors are introduced to analyze the motion trajectories.		
Y. Zhang et al.	2013	Modeling respiratory motion for reducing motion artifacts in 4D CT images	A patient-specific respiratory motion model, based on principal component analysis (PCA) of motion vectors obtained from deformable image registration, with the main goal of reducing image artifacts caused by irregular motion during 4D CT acquisition.	Displacement vector fields relative to a reference phase were calculated using an in-house deformable image registration method. The authors then used PCA to decompose each of the displacement vector fields into linear combinations of principal motion bases. These projections were parameterized using a spline model to allow the reconstruction of the displacement vector fields at any given phase in a respiratory cycle. Finally, the displacement vector fields were used to	The initial large discrepancies across the landmark pairs were significantly reduced after deformable registration, and the accuracy was similar to or better than that reported by state-of-the-art methods. The motion model was used to reduce irregular motion artifacts in the 4D CT images of three lung cancer patients. Visual assessment indicated that the proposed approach could reduce severe image artifacts.	The proposed approach can mitigate shape distortions of anatomy caused by irregular breathing motion during 4D CT acquisition.

				deform the reference CT image to synthesize CT images at the selected phase with much reduced image artifacts.		
B. Fuerst et al.	2014	Patient-Specific Biomechanical Model for the Prediction of Lung Motion From 4-D CT Images	An approach to predict the deformation of the lungs and surrounding organs during respiration.	A computational model of the respiratory system, which comprises an anatomical model extracted from computed tomography (CT) images at end-expiration (EE), and a biomechanical model of the respiratory physiology, including the material behavior and interactions between organs.	The method was then tested on five public datasets. Results showed that the model was able to predict the respiratory motion with an average landmark error of 3.40 ±1.0 mm over the entire respiratory cycle.	The estimated 3-D lung motion may constitute as an advanced 3-D surrogate for more accurate medical image reconstruction and patient respiratory analysis.

Appendix-D: Table D.1: Tabular Literature Survey, Chapter 5

Author	Year	Title	About	Method	Findings	Remarks
X. Pennec et al.	2005	Riemannian Elasticity: A Statistical Regularization Framework for Non-linear Registration	The elastic energy has been interpreted as the distance of the Green-St Venant strain tensor to the identity, which reflects the deviation of the local deformation from a rigid transformation.	By changing the Euclidean metric for a more suitable Riemannian one, a consistent statistical framework is defined to quantify the amount of deformation. These statistics are then used as parameters in a Mahalanobis distance to measure the statistical deviation from the observed variability, giving a new regularization criterion that we called the statistical Riemannian elasticity.	It was found that the new criterion is able to handle anisotropic deformations and is inverse-consistent.	Preliminary results showed that it can be quite easily implemented in a non-rigid registration algorithm.
B. Zhang et al.	2011	Three-dimensional elastic image registration based on strain energy minimization: application to prostate magnetic resonance imaging	A novel 3-D elastic registration procedure that is based on the minimization of a physically motivated strain energy function that requires the identification of similar features (points, curves, or surfaces) in the source and target images.	The Gauss-Seidel method was used in the numerical implementation of the registration algorithm. The registration procedure was validated on synthetic digital images, MR images from prostate phantom, and MR images obtained on patients. The	The registration error on patient data was 1.8 ± 0.7 pixels. Registration also improved image similarity (normalized cross-correlation) from 0.72 ± 0.10 to 0.96 ± 0.03 on patient data.	Registration results on prostate data in vivo demonstrated that the registration procedure could be used to significantly improve both the accuracy of localized therapies such as brachytherapy or external beam therapy and can be

				registration error, assessed by averaging the displacement of a fiducial landmark in the target to its corresponding point in the registered image.		valuable in the longitudinal follow-up of patients after therapy.
R.W.K. So et al.	2011	Non-rigid image registration of brain magnetic resonance images using graph-cuts	A graph-cut based method for non-rigid medical image registration on brain magnetic resonance images. The non-rigid medical image registration problem is reformulated as a discrete labelling problem.	Modelled the non-rigid registration as a multi-labeling problem by Markov random field. The image registration problem is therefore modeled by two energy terms based on intensity similarity and smoothness of the displacement field. The MRF energy is minimized by graph-cuts algorithm via α-expansions.	Compared the registration results of the proposed method with two state-of-the-art medical image registration approaches: free-form deformation based method and demons method. In addition, the registration results were also compared with that of the linear programming based image registration method.	The proposed method was found to be more robust against different challenging non-rigid registration cases with consistently higher registration accuracy than those three methods, and gives realistic recovered deformation fields.
A. R. Dykstra et al.	2012	Individualized localization and cortical surface-based registration of intracranial electrodes	A method which co-registers high-resolution preoperative MRI with postoperative computerized tomography (CT) for the purpose of individualized functional mapping of both normal	The method accurately (within 3 mm, on average) localizes electrodes with respect to an individual's neuroanatomy. Furthermore, we outline a principled procedure for either volumetric or	The method was demonstrated in five patients with medically-intractable epilepsy undergoing invasive monitoring of the seizure focus prior to its surgical removal.	The straight-forward application of this procedure to all types of intracranial electrodes, robustness to deformations in both skull and brain, and the ability to

			and pathological (e.g., interictal discharges and seizures) brain activity.	surface-based group analyses.	Accuracy was within 3mm of average.	compare electrode locations across groups of patients makes this procedure an important tool for basic scientists as well as clinicians.
H.P. Heinrich et al.	2013	MRF-Based Deformable Registration and Ventilation Estimation of Lung CT	Three major challenges associated with lung ct registration viz. large motion of small features, sliding motions between organs and changing image contrast due to compression are addressed and potentially higher quality of discrete approaches is preserved.	First, an image-derived minimum spanning tree is used as a simplified graph structure, which coped well with the complex sliding motion and allowed us to find the global optimum very efficiently. Second, a stochastic sampling approach for the similarity cost between images is introduced within a symmetric, diffeomorphic B-spline transformation model with diffusion regularization. The complexity is reduced by orders of magnitude and enables the minimization of much larger label spaces. In addition to the	The improvements are validated in accuracy and performance on exhale-inhale CT volume pairs using a large number of expert landmarks.	The three challenges posed in the beginning are met.

				geometric transform labels, hyper-labels are introduced, which represent local intensity variations in this task, and allow for the direct estimation of lung ventilation.		
K. Nakagomi et al.	2013	Multi-shape graph cuts with neighbour prior constraints and its application to lung segmentation from a chest CT volume	A novel graph cut algorithm that can take into account multi-shape constraints with neighbor prior constraints, and reports on a lung segmentation process from a three-dimensional computed tomography (CT) image based on this algorithm.	A novel segmentation algorithm that improves lung segmentation for cases in which the lung has a unique shape and pathologies such as pleural effusion by incorporating multiple shapes and prior information on neighbour structures in a graph cut framework.	The efficacy of the proposed algorithm is demonstrated by comparing it to conventional one using a synthetic image and clinical thoracic CT volumes.	--

Appendix-E: Table E.1: Track data for subject 'case 5' sagittal AP.

	Track_label	Track_duration	Track_start	Track_stop	Track_displacement	Track_x_location	Track_y_location	Track_mean_speed	Track_max_speed	Track_min_speed	Track_median_speed	Track_std_speed
1	Track_0	5	0	5	0.26	55.58	114.13	0.97	1.96	0.34	0.54	0.73
2	Track_1	5	0	5	14.33	99.35	110.7	3.2	4.87	1	3.69	1.77
3	Track_2	5	0	5	5.09	160.27	111.02	1.39	2.42	0.73	1.50	0.68
4	Track_3	5	0	5	2.93	187.64	112.85	1.64	3.53	0.66	1.09	1.22
5	Track_4	5	0	5	10.9	113.78	113.1	2.32	4.59	0.87	1.42	1.64
6	Track_5	5	0	5	0.24	264.41	115.45	0.6	1.17	0.28	0.55	0.35
7	Track_6	5	0	5	6.52	138.69	113.65	1.91	4.04	0.18	1.05	1.8
8	Track_7	5	0	5	1.5	319.22	122.76	1.21	1.92	0.35	1.22	0.72
9	Track_8	5	0	5	0.27	270.18	130.22	0.77	1.91	0	0.13	0.97
10	Track_9	5	0	5	0.77	8.18	125.81	0.99	2.09	0.24	0.62	0.78
11	Track_10	5	0	5	4.28	170.26	125.42	1.44	2.59	0.61	0.97	0.98
12	Track_11	5	0	5	0.55	271.08	132.75	0.62	1.8	0	0.38	0.69
13	Track_12	5	0	5	0.45	51.16	136.91	0.27	0.46	0.14	0.25	0.12
14	Track_13	4	0	4	0.46	323.07	133.45	1.41	2.39	0.66	1.9	0.87
15	Track_14	5	0	5	7.7	324.77	139.27	2.71	9.07	0.23	1.36	3.63
16	Track_15	5	0	5	2.27	231.29	134.51	1.27	2.42	0.65	0.95	0.73
17	Track_16	5	0	5	6.42	150.67	137.12	1.79	6.24	0.3	0.82	2.51
18	Track_17	5	0	5	0.26	273.80	138.70	0.4	0.74	0.25	0.34	0.2

	Track_label	Track_duration	Track_start	Track_stop	Track_displacement	Track_x_location	Track_y_location	Track_mean_speed	Track_max_speed	Track_min_speed	Track_median_speed	Track_std_speed
19	Track_18	5	0	5	3.42	232.33	146.68	2.04	2.91	0.71	2.26	0.93
20	Track_19	3	0	3	4.38	169.36	145.27	2.15	3.85	0.56	2.03	1.65
21	Track_20	4	0	4	3	203.69	143.52	1.27	2.89	0.31	1.51	1.21
22	Track_21	5	0	5	5.85	181.60	142.24	1.79	4.55	0.5	1.24	1.59
23	Track_22	5	0	5	1.1	326.97	146.73	0.56	0.98	0.06	0.56	0.33
24	Track_23	5	0	5	6.84	137.87	140.06	2.17	6.7	0.66	1.21	2.55
25	Track_24	5	0	5	0.73	8.86	150.87	0.54	1.31	0.09	0.38	0.47
26	Track_25	5	0	5	13.08	74.93	142.74	3.11	12.98	0.41	0.81	5.52
27	Track_26	5	0	5	0.63	50.12	155.37	0.29	0.48	0.07	0.28	0.15
28	Track_27	5	0	5	0.21	286.48	155.84	0.81	1.28	0.24	0.74	0.4
29	Track_28	5	0	5	7.55	156.12	149.82	2.89	7.1	0.71	2.26	2.61
30	Track_29	5	0	5	6.43	168.78	154.22	1.84	3.06	0.95	1.47	0.96
31	Track_30	5	0	5	0.9	330.28	160.52	2.16	2.88	0.29	2.77	1.1
32	Track_31	4	0	4	14	81.56	152.41	3.63	11.66	0.68	1.16	5.36
33	Track_32	5	0	5	1.63	289.19	162.56	3.99	8.81	0.22	1.99	3.85
34	Track_33	4	0	4	13.13	332.69	170.36	3.37	7.19	0.27	5.26	3.4
35	Track_34	4	0	4	10.59	140.99	163.05	2.66	4.72	1.34	3.19	1.62
36	Track_35	5	0	5	7.33	177.98	165.70	2.2	3.84	1.25	1.81	1.12
37	Track_36	5	0	5	0.58	333.06	171.77	0.73	1.32	0.02	0.74	0.58
38	Track_37	5	0	5	1.28	48.70	176.52	0.63	0.94	0.22	0.69	0.27
39	Track_38	5	0	5	12.9	129.53	166.71	2.76	5.21	0.43	2.15	2.09

	Track_label	Track_duration	Track_start	Track_stop	Track_displacement	Track_x_location	Track_y_location	Track_mean_speed	Track_max_speed	Track_min_speed	Track_median_speed	Track_std_speed
41	Track_40	4	0	4	8.59	159.05	173.06	2.32	4.94	0.72	2.55	1.92
42	Track_41	4	0	4	1.06	9.5	190.77	1.28	1.67	0.53	1.65	0.66
43	Track_42	5	0	5	2.58	8.75	187.31	2.75	6.64	0	1.52	3.16
44	Track_43	5	0	5	8.3	182.51	177.42	2.57	5.05	0.96	1.59	1.86
45	Track_44	1	0	1	5.49	113.58	180.31	5.49	5.49	5.49	5.49	NaN
46	Track_45	5	0	5	13.68	220.44	185.44	3.35	7.23	1.13	2.54	2.33
47	Track_46	5	0	5	1.95	293.02	184.74	0.56	1.35	0.04	0.45	0.57
48	Track_47	5	0	5	18.19	143.78	196.58	5.77	12.85	1.4	3.82	4.71
49	Track_48	5	0	5	1.4	47.88	195.51	1.8	3.68	0.12	1.72	1.46
50	Track_49	5	0	5	0.96	295.28	192.26	0.5	0.75	0.09	0.58	0.25
51	Track_50	5	0	5	1.74	335.92	187.98	0.75	1.62	0.21	0.69	0.54
52	Track_51	3	0	3	8.74	7.59	183.11	2.91	8.74	0	0	5.05
53	Track_52	5	0	5	16.36	337.83	202.19	4.57	9.92	0.74	2.5	3.85
54	Track_53	2	0	2	3.34	146.43	205.46	1.87	2.16	1.57	2.16	0.41
55	Track_54	5	0	5	0.13	9.4	204.24	0.63	1.18	0.21	0.74	0.43
56	Track_55	2	0	2	2.51	220.57	205.30	2.57	3.4	1.74	3.4	1.18
57	Track_56	5	0	5	0.94	338.14	203.95	3.17	5.92	0.93	2.25	2.18
58	Track_57	5	0	5	6.3	206.94	197.23	1.97	2.93	1.18	1.85	0.69
59	Track_58	5	0	5	15.61	131.91	196.09	3.21	7.54	1.22	2.2	2.5
60	Track_59	5	0	5	7.98	192.74	192.88	2.2	4.29	1.27	1.77	1.21
61	Track_60	5	0	5	3.31	47.03	214.16	0.86	2.99	0.08	0.43	1.21

	Track_label	Track_duration	Track_start	Track_stop	Track_displacement	Track_x_location	Track_y_location	Track_mean_speed	Track_max_speed	Track_min_speed	Track_median_speed	Track_std_speed
62	Track_61	5	0	5	0.54	8.61	214.38	0.52	1.03	0.04	0.5	0.48
63	Track_62	5	0	5	0.52	303.44	213.91	0.5	1.31	0.07	0.43	0.48
64	Track_63	5	0	5	12.58	224.74	206.36	4.88	8.03	2.2	4.61	2.23
65	Track_64	5	0	5	23.5	72.35	216.39	4.72	7.19	0.51	6.67	3.08
66	Track_65	5	0	5	16.63	130.4	219.84	3.87	7.32	2.02	3.24	2.22
67	Track_66	5	0	5	2.4	9	226.26	1.78	4.21	0.12	1.43	1.56
68	Track_67	5	0	5	16.8	159.58	214.9	3.42	7.59	0.35	2.23	3.3
69	Track_68	5	0	5	1.79	339	220.73	1.08	2.57	0.26	0.74	0.89
70	Track_69	2	0	2	10.37	134.56	216.35	5.45	8.47	2.43	8.47	4.27
72	Track_71	5	0	5	1.12	49.74	235.92	0.65	1.02	0.32	0.67	0.29
73	Track_72	5	0	5	0.31	9.59	239.52	0.43	0.78	0.1	0.49	0.3
74	Track_73	5	0	5	2.81	303.88	229.49	0.96	1.87	0.67	0.75	0.51
75	Track_74	5	0	5	21.98	118.8	220.1	4.49	7.92	0.44	3.9	3.26
76	Track_75	5	0	5	19.24	148.37	220.57	4.89	7.99	2.76	3.1	2.75
77	Track_76	5	0	5	8.33	250.39	243.77	3.82	7.39	0.08	4.32	2.66
78	Track_77	5	0	5	0.27	50	250.94	0.23	0.4	0.12	0.19	0.12
79	Track_78	5	0	5	14.28	202.3	233.74	4.46	9.2	0.93	3.46	3.77
80	Track_79	5	0	5	12.2	219.57	238.32	7.39	13.8	2.64	6.6	4.11
81	Track_80	5	0	5	2.72	339.94	245.24	1.17	3.89	0.13	0.33	1.57
82	Track_81	5	0	5	3.15	284.23	243.57	1.30	2.2	0.26	1.22	0.79
83	Track_82	5	0	5	21.98	122.63	245.86	5.03	13.55	1.47	1.79	5.21

	Track_label	Track_duration	Track_start	Track_stop	Track_displacement	Track_x_location	Track_y_location	Track_mean_speed	Track_max_speed	Track_min_speed	Track_median_speed	Track_std_speed
84	Track_83	3	0	3	4.63	266.26	251.83	2.22	5.14	0.45	1.09	2.54
85	Track_84	5	0	5	6.34	258.7	247.68	1.85	4.46	0.97	1.15	1.48
86	Track_85	5	0	5	17.12	188.53	245.2	5.38	10.93	0.44	3.71	4.52
87	Track_86	5	0	5	0.18	11.6	253.95	0.38	1.03	0.04	0.21	0.42
88	Track_87	2	0	2	3.83	341.28	265.75	2.56	4.46	0.67	4.46	2.69
89	Track_88	5	0	5	0.33	12.97	270.9	0.24	0.5	0.05	0.24	0.17
90	Track_89	5	0	5	20.98	175.78	252.71	4.6	12.03	1.53	3	4.22
91	Track_90	5	0	5	0.21	53.34	260.25	0.26	0.46	0.09	0.28	0.14
93	Track_92	5	0	5	0.52	16.20	302.02	0.21	0.54	0.04	0.14	0.20
94	Track_93	5	0	5	4.29	346.99	298.99	1.46	3.8	0.27	1.08	1.39
95	Track_94	5	0	5	0.13	60.22	289.99	0.19	0.26	0.07	0.21	0.08
96	Track_95	5	0	5	27.14	93.69	280.63	5.43	11.19	1.4	3.13	4.55
98	Track_97	5	0	5	1.96	344.13	282.58	1.18	2.77	0.47	0.69	0.96
99	Track_98	5	0	5	0.86	112.24	7.41	0.18	0.32	0.07	0.18	0.09
102	Track_101	5	0	5	0.91	19.46	11.41	2.01	4.57	0	1.01	1.95
103	Track_102	5	0	5	1.36	139.31	11.53	0.35	0.77	0.06	0.12	0.34
104	Track_103	5	0	5	17.81	342.38	272.59	3.66	8.23	0.22	1.43	3.93
105	Track_104	5	0	5	0.78	126.55	7.76	0.48	1.52	0.06	0.07	0.65
106	Track_105	5	0	5	22.83	102.94	261.32	4.59	14.91	0.91	2.99	5.88
107	Track_106	4	0	4	17.17	161.35	266.23	6.38	11.75	1.18	10.52	5.52

	Track_label	Track_duration	Track_start	Track_stop	Track_displacement	Track_x_location	Track_y_location	Track_mean_speed	Track_max_speed	Track_min_speed	Track_median_speed	Track_std_speed
108	Track_107	5	0	5	0.12	58.68	273.71	0.34	0.74	0.03	0.15	0.33
109	Track_108	5	0	5	0.48	15.2	280.86	0.64	1.67	0.17	0.45	0.61
110	Track_109	5	0	5	2.43	93.57	17.05	0.78	1.25	0.12	0.66	0.48
111	Track_110	5	0	5	5.9	267.84	17.04	2.18	3.87	0	2.3	1.39
112	Track_111	5	0	5	0.59	161.01	23.23	0.38	0.55	0.1	0.42	0.2
113	Track_112	5	0	5	0.57	15.07	23.49	0.14	0.28	0.07	0.11	0.09
114	Track_113	5	0	5	23.73	88.74	326.64	5.25	12.97	1	4.09	4.54
115	Track_114	5	0	5	1.55	87.2	25.72	0.36	0.7	0.13	0.34	0.24
116	Track_115	5	0	5	5.34	65.33	334.38	1.08	2.11	0.55	0.95	0.62
117	Track_116	5	0	5	11.88	269.5	20.07	4.44	7.49	0.27	4.88	2.61
118	Track_117	5	0	5	1.5	101.65	12.63	0.45	0.91	0.08	0.32	0.4
119	Track_118	5	0	5	2.61	265.42	12.41	0.7	1.78	0.05	0.82	0.8
120	Track_119	2	0	2	0.42	18.92	13.11	0.21	0.42	0	0.42	0.29
121	Track_120	5	0	5	1.42	23.71	331.56	0.75	1.17	0.48	0.61	0.3
122	Track_121	5	0	5	3.67	266.22	13.85	1.72	3.29	0.61	1.78	1.13
123	Track_122	5	0	5	0.86	148.79	16.17	0.24	0.58	0.04	0.15	0.21
124	Track_123	5	0	5	5.21	350.67	320.89	2.52	8.22	0.32	1.62	3.26
125	Track_124	3	0	3	0.04	274.51	29.69	7.72	11.6	0.23	11.33	6.49
127	Track_126	5	0	5	0.43	17.89	314.51	0.17	0.4	0.01	0.18	0.15
128	Track_127	5	0	5	1.02	75.39	39.33	1.60	2.56	0.46	2.12	1.04
129	Track_128	5	0	5	0.57	63.53	323.35	1.32	1.97	0.31	1.42	0.7

	Track_label	Track_duration	Track_start	Track_stop	Track_displacement	Track_x_location	Track_y_location	Track_mean_speed	Track_max_speed	Track_min_speed	Track_median_speed	Track_std_speed
130	Track_129	5	0	5	14.75	349.37	313.01	3.45	5.63	1.25	4.18	2.01
131	Track_130	5	0	5	26.24	99.35	313.94	7.46	13.61	0.71	7.91	4.88
132	Track_131	5	0	5	0.12	280.12	41.08	0.15	0.27	0.06	0.14	0.09
133	Track_132	5	0	5	1.94	165.9	26.92	0.42	1.3	0.04	0.27	0.51
134	Track_133	5	0	5	13	348.35	307.13	3.93	9.25	1.48	1.95	3.31
135	Track_134	5	0	5	7.08	273.32	27.35	6.06	11.41	0.09	7.25	5.64
136	Track_135	5	0	5	0.91	172.18	31.78	0.3	0.39	0.09	0.37	0.13
137	Track_136	5	0	5	28.77	109.73	304.07	7.14	12.20	0.71	6.88	4.23
138	Track_137	5	0	5	0.53	66.46	312.42	0.22	0.27	0.09	0.24	0.07
139	Track_138	5	0	5	3.78	109.2	57.81	0.86	1.69	0.39	0.71	0.49
140	Track_139	5	0	5	2.30	354.66	367.15	1.67	2.62	0.63	1.54	0.89
141	Track_140	5	0	5	0.47	67.93	57.83	2.86	6.36	0.45	3.61	2.7
142	Track_141	5	0	5	0.84	207.48	56.88	0.24	0.63	0.11	0.16	0.22
143	Track_142	5	0	5	6.89	11.65	59.83	1.45	4.64	0.18	0.44	1.89
144	Track_143	3	0	3	0.04	285.35	51.72	0.51	0.77	0.28	0.47	0.25
145	Track_144	5	0	5	5.17	137.49	51.54	1.11	2.47	0.23	0.85	0.86
147	Track_146	4	0	4	1.14	196.07	48.82	0.51	0.95	0.18	0.57	0.33
148	Track_147	5	0	5	2.1	21.23	361.50	0.99	1.45	0.24	1.43	0.58
149	Track_148	5	0	5	32.22	82.45	339.28	6.72	12.09	2.52	5.28	3.75
150	Track_149	5	0	5	1.4	20.37	355.26	0.49	0.73	0.05	0.49	0.26
151	Track_150	5	0	5	0.53	186.46	42.1	0.47	0.88	0.19	0.44	0.26

	Track_label	Track_duration	Track_start	Track_stop	Track_displacement	Track_x_location	Track_y_location	Track_mean_speed	Track_max_speed	Track_min_speed	Track_median_speed	Track_std_speed
152	Track_151	5	0	5	0.16	12.29	40.84	1.03	2.51	0.24	0.71	0.91
153	Track_152	2	0	2	2.78	67.71	350.67	1.4	1.94	0.87	1.94	0.76
154	Track_153	5	0	5	3.04	236.06	80	0.68	1.25	0.21	0.75	0.41
155	Track_154	5	0	5	3.66	293.54	69.27	2.37	4.71	0.2	3.01	1.93
156	Track_155	5	0	5	5.89	295.36	73.1	7.42	10.36	4.47	9	2.73
157	Track_156	5	0	5	6.81	97.02	67.06	1.45	2.03	0.34	1.49	0.69
158	Track_157	5	0	5	11.77	294.65	71.48	4.26	13.14	1.07	2.3	5
160	Track_159	5	0	5	6.51	353.73	342.75	2.65	5.06	1.58	1.81	1.46
161	Track_160	5	0	5	0.34	64.57	67.3	0.24	0.49	0.02	0.16	0.22
164	Track_163	5	0	5	6.32	115.16	88.62	1.51	2.64	0.75	1.03	0.9
165	Track_164	5	0	5	1.16	244.25	93.56	0.4	0.63	0.21	0.41	0.16
166	Track_165	5	0	5	2.7	151.41	91.27	1.25	1.85	0.78	1.08	0.49
168	Track_167	5	0	5	0.22	305.18	392.1	0.53	1.21	0.12	0.39	0.44
169	Track_168	5	0	5	3.71	316.59	392.18	0.74	1.02	0.24	0.93	0.35
170	Track_169	5	0	5	7.67	336.78	392.23	2.83	4.74	0.73	3.23	2.01
172	Track_171	5	0	5	13.36	262.07	392.14	3.90	5.4	1.96	4.24	1.38
173	Track_172	5	0	5	11	239.78	392.17	3.29	4.64	1.45	3.8	1.24
174	Track_173	5	0	5	4.58	284.9	392.14	3.74	8.77	0.5	2.86	3.28
175	Track_174	3	0	3	1.18	272.8	392.13	4.55	7.41	1.72	4.51	2.84

	Track_label	Track_duration	Track_start	Track_stop	Track_displacement	Track_x_location	Track_y_location	Track_mean_speed	Track_max_speed	Track_min_speed	Track_median_speed	Track_std_speed
176	Track_175	4	0	4	0.27	298.56	79.61	0.82	1.57	0.20	1.17	0.66
177	Track_176	5	0	5	15.96	210.15	392.18	3.81	10.97	0.07	1.52	4.71
178	Track_177	5	0	5	0.59	7.80	82.33	0.18	0.55	0.01	0.09	0.22
179	Track_178	5	0	5	4.02	189.59	392.13	1.03	2.78	0.09	0.59	1.04
181	Track_180	5	0	5	0.32	189.81	78.59	1.45	2.75	0.16	1.27	1.05
182	Track_181	4	0	4	7.54	102.52	76.17	1.75	2.7	0.57	1.97	1.09
183	Track_182	3	0	3	5.51	142.34	392.15	1.84	3.04	0.62	1.86	1.21
184	Track_183	5	0	5	9.56	176.94	392.12	4.51	13.19	0.41	3.38	5.92
185	Track_184	5	0	5	8.35	164.04	392.14	2.67	7.89	0.02	2.49	3.18
186	Track_185	5	0	5	0.91	61.99	80.08	0.49	0.75	0.29	0.48	0.17
187	Track_186	5	0	5	0.3	94.97	392.13	0.31	0.41	0.21	0.33	0.09
188	Track_187	5	0	5	0.73	84.73	392.17	0.27	0.43	0.12	0.27	0.12
189	Track_188	5	0	5	8.72	130.02	392.14	2.06	7.91	0.02	0.77	3.3
190	Track_189	5	0	5	3.7	116.09	392.15	4.33	11.46	1.22	2.65	4.1
191	Track_190	5	0	5	1.28	312.97	107.75	1.54	3.59	0	0.86	1.75
192	Track_191	5	0	5	0.27	56.67	392.1	0.41	0.86	0.04	0.39	0.36
193	Track_192	5	0	5	0.24	66.68	392.14	0.33	0.45	0.17	0.31	0.11
194	Track_193	5	0	5	0.06	33.04	391.97	0.03	0.05	0.01	0.02	0.02
195	Track_194	5	0	5	6.08	314.51	111.68	4.06	7.11	0	3.95	2.77
196	Track_195	5	0	5	1.21	7.21	105.67	0.89	1.03	0.66	0.97	0.16
197	Track_196	5	0	5	9.24	307.4	95.57	2.11	9.39	0.06	0.38	4.07

	Track_label	Track_duration	Track_start	Track_stop	Track_displacement	Track_x_location	Track_y_location	Track_mean_speed	Track_max_speed	Track_min_speed	Track_median_speed	Track_std_speed
198	Track_197	5	0	5	1.61	59.02	97.7	0.58	0.96	0.32	0.58	0.25
199	Track_198	2	0	2	5.54	195.37	93.01	3	5.59	0.42	5.59	3.66
200	Track_199	5	0	5	1.46	177.49	95.71	0.99	1.32	0.39	1.06	0.37
201	Track_200	5	0	5	0.12	24.42	369.15	0.37	0.88	0.1	0.29	0.3
202	Track_201	3	1	4	5.8	293.54	392.14	2.62	6.82	0.23	0.8	3.65
203	Track_202	4	1	5	0.43	285.31	51.76	0.32	0.47	0.14	0.38	0.15
204	Track_203	4	1	5	2.97	126.64	39.73	0.82	1.7	0.1	0.79	0.66
205	Track_204	4	1	5	1.26	294.09	70.43	6.72	11.67	2.3	10.32	4.97
206	Track_205	4	1	5	0.55	218.61	57.98	0.26	0.38	0.15	0.3	0.1
208	Track_207	4	1	5	2	47.88	221.05	1.07	2.53	0.36	0.75	0.99
209	Track_208	4	1	5	4.18	234.02	239.71	4.06	5.35	2.31	4.93	1.37
211	Track_210	4	1	5	11.82	108.74	170.77	3.87	7.38	1.65	4.7	2.74
212	Track_211	4	1	5	3.16	18.39	14.75	0.93	3.16	0	0.27	1.5
213	Track_212	4	1	5	12.8	154.66	205.48	3.55	5.94	1.86	3.58	1.74
214	Track_213	4	1	5	0.74	62.44	299.05	0.64	1.03	0.31	0.63	0.3
216	Track_215	3	2	5	8.8	344.93	285.62	5.22	11.75	0.47	3.43	5.85
219	Track_218	3	2	5	11.87	164.1	255.73	4.81	8.87	1.68	3.87	3.69
220	Track_219	3	2	5	1.45	75.43	39.32	0.94	2.12	0.23	0.46	1.03
222	Track_221	3	2	5	1	75.01	40.21	1.69	3.03	0.67	1.37	1.21
223	Track_222	3	2	5	1.57	154.9	392.14	1.23	1.95	0.68	1.06	0.66
224	Track_223	3	2	5	1.35	137.98	121.22	1.02	1.61	0.65	0.80	0.52

	Track_label	Track_duration	Track_start	Track_stop	Track_displacement	Track_x_location	Track_y_location	Track_mean_speed	Track_max_speed	Track_min_speed	Track_median_speed	Track_std_speed
226	Track_225	3	2	5	5.41	312.13	105.92	2.09	5.29	0.48	0.51	2.77
227	Track_226	3	2	5	4.2	245.61	217.09	3.52	6.23	0.47	3.86	2.9
228	Track_227	2	2	4	0.37	293.99	187.58	0.37	0.55	0.19	0.55	0.25
229	Track_228	3	2	5	5.94	153.42	178.74	4.01	7.16	1.48	3.38	2.89
230	Track_229	3	2	5	13.64	147.34	188.86	5.57	8.2	1.43	7.07	3.63
231	Track_230	2	3	5	18.36	111.38	294.26	9.58	13.99	5.17	13.99	6.24
232	Track_231	2	3	5	5.94	143.72	270.03	2.97	3.09	2.85	3.09	0.17
233	Track_232	2	3	5	9.26	129.44	278.8	5.28	8.57	1.99	8.57	4.66
234	Track_233	2	3	5	1.4	289.31	60.99	0.71	1.24	0.18	1.24	0.75
235	Track_234	2	3	5	6.57	188.51	181.98	3.61	3.93	3.29	3.93	0.45
236	Track_235	2	3	5	2.08	323.06	133.87	1.26	2.28	0.25	2.28	1.44
237	Track_236	2	3	5	0.61	330.39	160.87	2.09	2.16	2.03	2.16	0.09
240	Track_239	2	3	5	10.5	205.37	392.17	5.25	10.09	0.41	10.09	6.84
241	Track_240	2	3	5	1.42	354.17	355.49	0.71	1.18	0.24	1.18	0.67
242	Track_241	2	3	5	22.34	352.25	334.21	11.17	14.38	7.97	14.38	4.53